CNS&E

Current Natural Sciences & Engineering
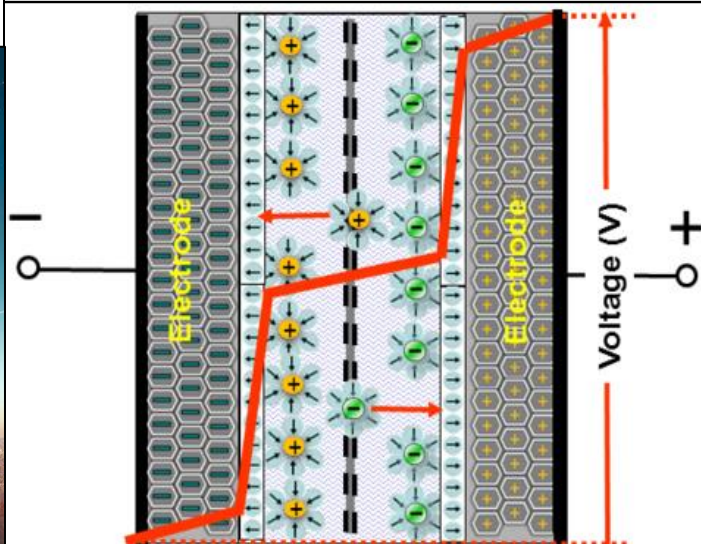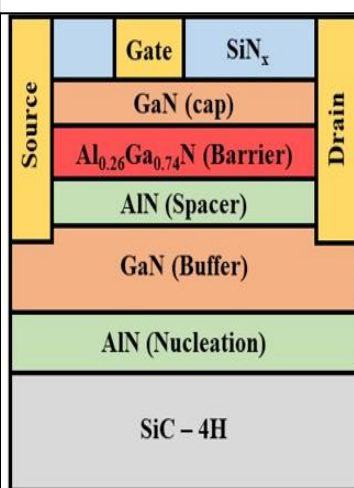
Multiple Input Multiple Output (MIMO) Antennas for Wireless Communication Channels

Improved Hybrid Supercapacitors
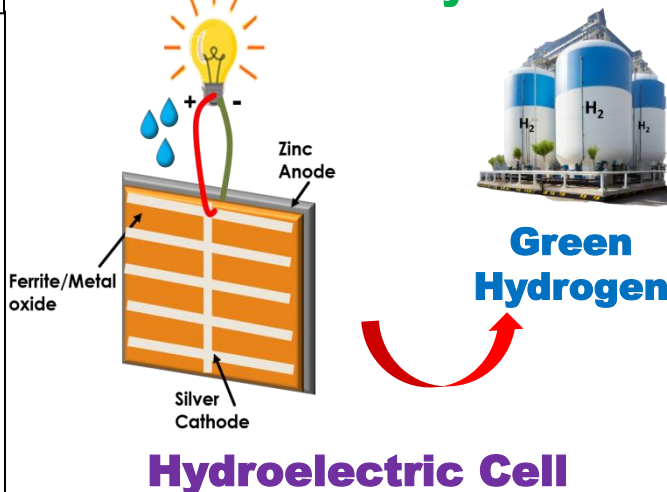

Conventional HEMT

SSC-FP HEMT

Green Electricity

Green Hydrogen

Hydroelectric Cell
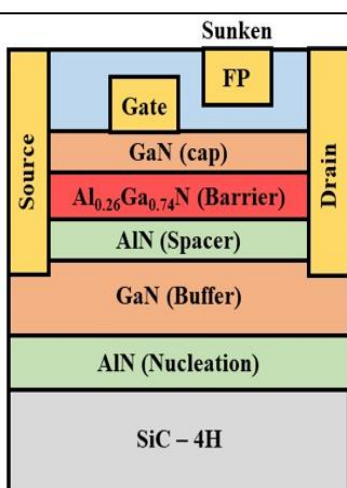
Conventional vs SSC-FP HEMT Device

Water splitting by Ferrite as Energy Material

About CNS&E

Current Natural Science & Engineering (CNS&E) Journal publishes new, innovative and cutting-edge research in Natural sciences including physical, chemical, biological, agricultural and environmental sciences, metrology, and other related interdisciplinary fields. Scientific research results in the form of high-quality manuscripts, review articles, mini-reviews, reports, news and short communications are highly welcome.

CNS&E is an Open Access, bimonthly, multidisciplinary journal published by the Vigyanvardhan Blessed Foundation (VBF), a non-profit organization working to disseminate science for the betterment of society.

Scope: CNS&E journal has a broad multidimensional scope. It publishes research in the areas of:
- ❑ Hydrogen & Renewable Energy
- ❑ Environmental Sciences & Hydroelectric Cell
- ❑ Artificial Intelligence Convergence in S&T
- ❑ Net Carbon Zero &Earth Sustainability
- ❑ Condensed Matter & Nanomaterials
- ❑ Health Science & Technology
- ❑ Nuclear Science: Health & Society
- ❑ Measurement Science & Industrial Research
- ❑ Digital & Sustainable Agriculture
- ❑ Smart Engineering Materials & Sensors

Publication Policy: The journal maintains integrity and high ethical values. Submitted manuscripts are peer-reviewed and evaluated for novel scientific content irrespective of its origin. The information about a submitted manuscript will be confidential and will not be disclosed other than Chief Editor, editorial staff, corresponding author, reviewers, and the publisher. The journal ensures that any unpublished work must not be used in Editor's, and reviewer's own research without the explicit written consent of the author(s).

Publication Decisions: The Chief Editor of the journal is responsible for deciding the publication or rejection of the submitted manuscript. The Chief Editor may take suggestion with other editors or reviewers in making decision.

Publisher: VB Foundation

CNS&E Volume 1, Issue 6, December 2024

Table of contents:

Advanced Materials: A Revolution for Environmental Sustainability

Prof R K Kotnala

Fnasc, Figu, Fmsi

Chief Editor, Current Natural Sciences & Engineering, Journal (CNS&E)

DOI: https://doi.org/10.63015/kotnala.2024.1.6

*Corresponding Author Email: rkkotnala@gmail.com

In today's world, materials are fundamental to every aspect of human existence. From the homes we inhabit to the technology we use, materials shape our lives. While we often take them for granted, advanced materials are driving groundbreaking advancements across various sectors. Scientists are now able to manipulate matter at the atomic level, creating novel materials with unprecedented properties. This has led to remarkable breakthroughs in the fields like:

- **Energy:** From renewable energy sources to energy storage solutions, advanced materials are crucial for addressing global energy challenges.
- **Environmental Sustainability:** Advanced materials play a vital role in developing sustainable solutions for environmental challenges, such as water purification, pollution control, and renewable energy generation.
- Recently, a new energy material nanoporous oxygen deficient ferrite has been invented to generate green electricity & hydrogen by Hydroelectric Cell, which is most suitable to accomplish Net Zero Carbon by water splitting only. It is an alternative to Solar Cell & Fuel Cell !
- **Healthcare:** Advanced materials are revolutionizing medical treatments, enabling the development of biocompatible implants, drug delivery systems, and diagnostic tools.
- **Electronics:** The rapid advancement of electronics relies heavily on the development of new materials with superior conductivity, flexibility, and efficiency.

The development and application of advanced materials are essential for human progress. By pushing the boundaries of materials science, we can create a future where technology serves humanity and enhances our quality of life while minimizing our impact on the environment.

I feel privileged to write a preface on "Advanced Materials: A Revolution for Environmental Sustainability." For our basic living energy, environment, water, shelter and good health are of paramount importance, that is heavily dependent on different types of materials usage besides the dire need of machines, communication & transportation means are also inevitable. Advanced materials are specially engineered substances with enhanced extraordinary properties, making them integral to various high-tech industries. They are widely used in sectors such as aerospace, healthcare, nuclear science, electronics, energy, and transportation. The rapid technological innovations and latest breakthroughs in material science lead to scientific advancements that are essential to keep pace with the human mind. Surprisingly, the recent revolutionary invention of a new energy material nanoporous oxygen deficient ferrite based Hydroelectric Cell that generates green electricity and hydrogen and it has been well taken globally as an invaluable gateway into the forefront of materials science. However, certain advanced functional materials for sustainable environment also play a big role in the welfare of humanity towards a greener and more ecologically balanced world. The role of radioisotopes is vital for our healthcare besides their applications as radio tracer techniques, agriculture and industries.

The sixth issue of CNS&E journal comprises of handpicked manuscripts that are highlighting an elaborative exploration of the most current material science research in the realm of the functional materials, with a specific focus on their applications in Wireless Communication Channels, Cobalt diselenide ternary Composite-based Supercapacitor, AlGaN/GaN High Electron Mobility Transistors (HEMTs), Radiation Dose Estimation from Uranium Mill Tailings Bricks, Disease Detection using Artificial Neural Network, Numerical Approximation Methods, and environmental monitoring. The phenomenal progress in science and technology has propelled us to innovate new materials frontier in this era of nanomaterials designed for extraordinary properties and ultimately CNS&E Journal is striving hard to support this cause.

Experimental Evaluation of MIMO Channel Capacity for Wireless Communication Channels

Shailesh, Vanshika Bhateja, Puneet Sehgal, Vipul Kaushal, and Kamlesh Patel*

Department of Electronic Science, University of Delhi South Campus, New Delhi, 110021, India

*Correspondence Author Email: kpatel@south.du.ac.in

Abstract: This research evaluates the channel capacity (CC) of 5th Generation Multiple Input Multiple Output (MIMO) antennas for propagation channels used in wireless communication. In the presence of several frequency sources for the information and communication channels, the effect on the CC of one-port and multi-port antennas is observed using the Path Loss Model (PLM), which is significantly impacted due to the number of antennas used and their characteristics. The CC is also estimated using a different approach, Kronecker's Model (KM). The channel matrix using both models is estimated by maintaining 5 cm and 25 cm spacing between the transmitting and receiving antennas. At 2.4 GHz for a 1-port antenna-based channel, the CC calculated using PLM is 5.5 bps/Hz for both spacing, whereas the CC calculated using KM is 3.65 bps/Hz and 3.12 bps/Hz for 5 cm and 25 cm spacing, respectively. The CC in the PLM is found between 35 to 140 bps/Hz at a frequency of 3.5 GHz, whereas it is reported between 12 to 38 bps/Hz using the KM at the same frequency, irrespective of distances. The maximum CC calculated using PLM is 5 bps/Hz for a 1-port antenna-based channel, 34 bps/Hz for 2-port MIMO antenna-based channels, 80 bps/Hz for 4-port MIMO antenna-based channels, and 157 bps/Hz for 8-port MIMO antenna based channels in the frequency band from 3.45 GHz to 3.7 GHz. Thus, it is experimentally confirmed that the capacity enriched by approximately 4 times on increasing the number of antenna ports from 2 to 8 and operating frequency.

1

1. Introduction: The rise of wireless personal communication systems (PCS) can be ascribed to the increasing demand for technological breakthroughs that more closely correspond with the swiftly evolving demands of our surroundings [1]. The idea of information and communication propagation channels, which have a wide range of applications in security, entertainment, healthcare, and communication, was conceived by one of the numerous inventive PCSs. Wireless communication networks such as Wireless Local Area Networks (WLAN), Worldwide Interoperability for Microwave Access (WiMAX), and 5G have been widely utilised by portable wireless communication devices. These are the most well-documented wireless bands used with MIMO antenna systems for large throughput [2]. Several MIMO antenna approaches have been developed recently to meet the requirements of the wireless communication system's channel capacity (CC) and data transmission rate [3]. Benefits of MIMO in WLAN and 5G technologies include faster data rates, a single connection, lower latency, and more connected nodes. The increasing demand for higher data rates has prompted the development of new techniques aimed at achieving these speeds. Unlike typical wireless propagation channels, the estimation of its characteristics in information and communication is influenced by the kind, orientation, propagation environment, and number of antenna elements [1].

Recently, a dielectric medium-equipped four-port integrated MIMO antenna construction

operating at 2.4 GHz was presented in [4]. By raising the pattern gain, the achievable CC (21 bps/Hz) was greater than the optimum CC. A dual-band 4-port MIMO antenna operating at 28 GHz and 41.69 GHz was proposed [5]. After evaluation, the CC was found to be nearly equal to 21 bps/Hz. A quad-port MIMO antenna with a 2.42–7.45 GHz bandwidth was suggested [6]. Considering that the four elements had different numbers of transmitting and receiving antennas, their maximum CC was 21.34 bps/Hz. A quad-element MIMO antenna for the 433 MHz industrial, scientific, and medical (ISM) bands was designed [7]. Moreover, this antenna offered 19.9 bps/Hz of CC. A range of the computed CC was reported 57.98 to 59.87 bps/Hz in a 12×12 MIMO antenna system made using four tri-port antennas [8]. A weighted polarisation MIMO antenna was used for 2.45 GHz wireless body area networks [9]. The average CC that was computed was 16 bps/Hz. In all the above-reported studies, CC is plotted by adjusting signal-to-noise ratio (SNR) values from 1 dB to 20 dB or taking any constant SNR value. So, there is very little information about the measurement of SNR, as well as the measurement of path loss and channel matrix [6].

This research uses a Spectrum Analyzer to obtain the received power and SNR which are used to evaluate the CC of WLAN/5G MIMO antennas under two different models: the Path Loss Model (PLM) and the Kronecker Model (KM). Additionally, by putting 1-port, 2-port, 4-port, and 8-port antennas at both the transmitting (T_x) and receiving (R_x) sides, the CC has been assessed. To the best of the authors' information, no thorough investigation has been done on the SNR and CC measurement for WLAN/5G MIMO. The rest of the research paper is structured as follows. The specifications of the measurement setup are highlighted in Section 2. The channel model and capacity estimates are provided in Section 3. In Section 4, the measured data for the SNR and CC are presented. In Section 4, the suggested work is

also contrasted with other reported work. The conclusion is provided in Section 5.

2. Measurement Setup: Three antennas, a 1-port circular spilt-ring resonator (SRR) antenna [10] (Ant. 1) for the WLAN band measurements over frequency band 2.29-2.95 GHz, a 2-port dual polarized circular slot microstrip antenna [11] (Ant. 2), and 8-port circular slot microstrip MIMO antenna [12](Ant. 3) for 5G band measurements over the frequency band 3.4-3.7 GHz are selected to form channels. These antennas are shown in Figure 1(a)-(c), respectively. These antennas provide sufficient gain and radiation properties in the entire WLAN (Ant. 1) and 5G band (Ant. 2, and Ant. 3). The ANSYS 3D High-Frequency Simulation Software (HFSS) is used for designing Ant. 1 and CST studio suite is for designing Ant. 2 and Ant. 3. These antennas are made on an FR4 substrate with 4.4 dielectric constant. The FR4 substrate is chosen for the antennas used because it is lightweight, cheap, and easily accessible, and its hardness makes this substrate immune to environmental changes. The main drawback of FR4 is that the copper coating on the FR4 substrate can be chipped off over time. The complete dimensions of the antennas used are shown in Table 1 and their performance parameters are presented in Table 2.

(a)   (b)

(c)
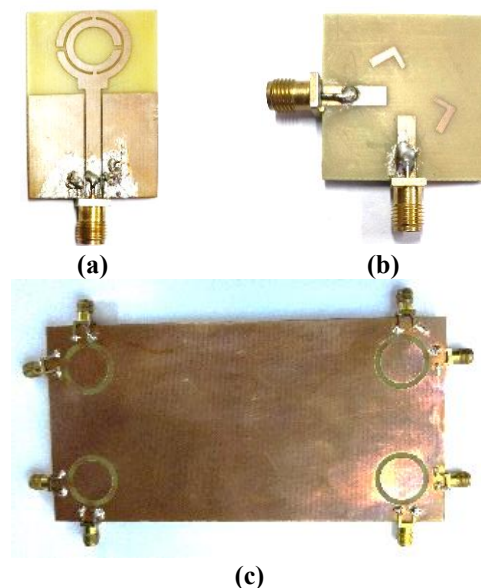
Figure 1: Fabricated picture of the antennas used (a) Ant. 1, (b) Ant. 2, and (c) Ant. 3.

An anechoic chamber was used for all the measurements, which has a size of 5.8m×2.7m×3.05m. This anechoic chamber has a Quiet Zone of size 0.4m×0.4m×0.4m, which provides a reflectivity level from -34.24 dB to -48.51 dB and shielding effectiveness from -86 dB to -90 dB in the frequency range 800 MHz -16 GHz. The standard used for the measurement is a ridge horn antenna. For all the measurements, two arbitrary distances (D) between identical transmitting and receiving antennas are selected as 5 and 25 cm, so the effect of distance over the CC can be observed in near-field and far-field regions.

Table 1: Complete dimensions of the antennas used

Antenna No.	Ant. 1	Ant. 2	Ant. 3
Feed (mm²)	22×3	11.9×3.5	11.9×3.5
Radius of the circular ring/slot (mm)	7.5 (external ring), 5.5 (internal ring)	8.1 (circular slot)	8.1 (circular slot)
Thickness of the circular ring/slot (mm)	1 (both rings)	1.6 (circular slot)	1.6 (circular slot)
Ground (mm²)	22×11	3.5×3.5	150×75
L-shaped structure	-	(5.5×1.5)+ (4.5×1)	(5.5×1.5)+ (4.5×1)

Table 2: Performance details of the antennas used

Antenna No.	Ant. 1	Ant. 2	Ant. 3
No. of ports	1	2	4/8
Structure of Antenna	Circular SRR	Circular Slot MIMO	Circular Slot MIMO
Frequency range (GHz)	2.29-2.95	3.4-3.7	3.4-3.8
Isolation (dB)	Not Applicable	-44.53	-12
Gain (dB)	2.1	3.77	5.21
Dimension (mm×mm)	43 ×26	35×35	75×150

For the measurements of signal-to-noise ratio (SNR) at these two distances, a RIGOL signal generator model DSG3060 is used to transmit the signal at the desired bands and an R&S spectrum analyzer model FSL6 is used to measure the SNR. To obtain the path loss values, an R&S handheld vector network analyser (VNA) ZVH8 is used for obtaining measured S-parameters for different sets of Ant. 1, Ant. 2, and Ant. 3 [11].

(a)

(b)

(c)

(d)

Figure 2: SNR measurement arrangements for (a) Block diagram, (b) Ant. 1 as 1T×1R at 5 cm, (c) Ant. 2 as 2T×2R at 25 cm, and (d) Ant. 3 as 8T×8R at 5 cm.

The channel (H)-matrix for channels made using these antennas is calculated from the respective path loss values using equation (2). Figure 2 illustrates a signal-to-noise ratio (SNR) measurement setup of how the antennas were p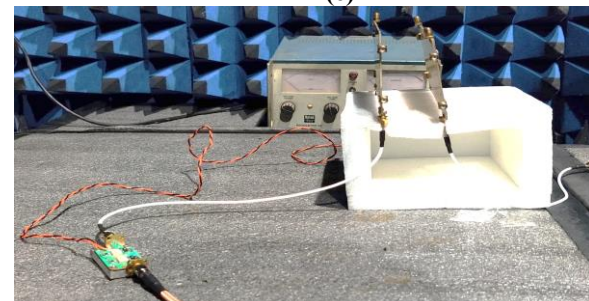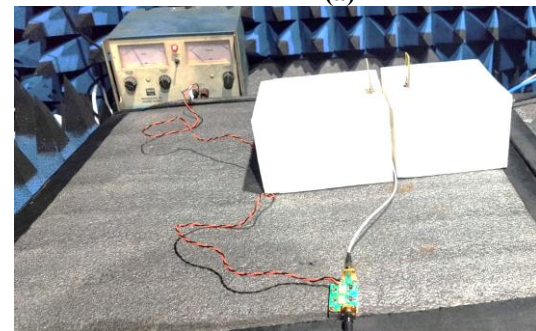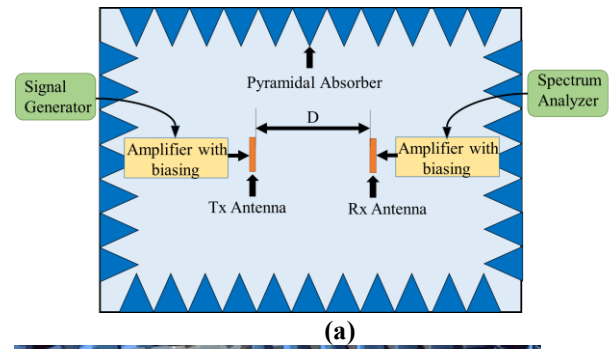laced for the wireless communication channels. An amplifier (green-colored circuit) is used to amplify the received signal and then measured on the spectrum analyzer. Since the transmission coefficient is a ratio, the gain of the signal due to this amplifier is nullified as appears equally in the incident and transmitted signals.

3. Characterization of MIMO Channel

3.1 Channel Model in MIMO: Unlike traditional Single-Input-Single-Output (SISO) (Figure 3(a)), a MIMO system (Figure 3(b)) allows for multiple independent transmission channels, without any additional transmitted power or bandwidth. This results in a CC that increases almost linearly with the increase in the number of antenna elements (under specific conditions) [13] [14].

The input-output relationship between the transmitter (T_x) and receiver (R_x) in a MIMO wireless propagation channel with m transmit and n receive antennas is expressed by [1],

$$Y = HX + W \tag{1}$$

where X=[m×1] transmit vector, Y= [n×1] received vector, W= additive white Gaussian noise vector, and H=[n×m] channel matrix composed of the complex random variable, h_{ij} for i=1,…., n and j=1,….m, signifying the channel fading coefficient between the ith receive antenna and jth transmit antenna.

3.2. Path Loss between Transmitter and Receiver: The scattering parameters (S-parameters) between T_x and R_x antennas can be obtained from a vector network analyzer (VNA), which gives the path loss (PL) using equation (1) [15].

$$PL = \frac{|S_{21}|^2}{(1-|S_{11}|^2)(1-|S_{22}|^2)g_{Tx}g_{Rx}e_p} \tag{2}$$

where S_{21} is the transmission coefficient, S_{11} and S_{22} are the reflection coefficients of T_x and R_x antennas, g_{TX} is the T_x antenna gain, g_{RX} is the R_x antenna gain, and e_p is polarization efficiency (=1 for co-polarized antennas and 0.5 for cross-polarized antennas). In another way, the PL is taken as the path gain factor= $\left(\lambda/_{4\pi D}\right)^2$, here D is the distance between T_x and R_x antennas, and λ is the wavelength. The channel matrix (H) formed between the T_x and R_x antennas is calculated using the PLM as follows [16]:

$$PL = -10\left(\frac{1}{MN}\sum_f 1 \sum_{i=1}^{M} 1 \sum_{j=1}^{N} |H_{i,j}(f)|^2\right) \tag{3}$$

where $H_{i,j}(f)$ is the transfer function in frequency-domain for the channel between the jth T_x antenna to ith R_x antenna, so it represents the channel formed between the T_x and R_x antennas, M, N=1, 2, 4,8.
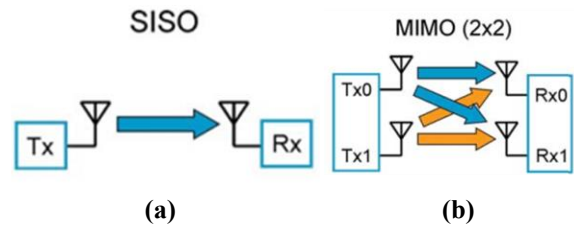
Figure 3: Techniques of channel communications with their CC (a) SISO (b) MIMO.

3.3 Kronecker Model (KM) for H-Matrix: Another model that can be used to construct the H-matrix is the Kronecker model (KM), which assumes that the CC is calculated in the propagation environment of an independent and identically distributed (i.i.d.) Rayleigh fading channel (H_w). This model considered that the complex Gaussian values with zero mean and unit variance make up the entries of the H_w matrix. Using the KM, the MIMO channel matrix H is provided by [17]:

$$H = R_r^{1/2} H_w R_t^{1/2} \tag{4}$$

where the transmission and reception matrices are denoted by Rt (=$\Lambda^{1/2}\overline{Rr}\,\Lambda^{1/2}$) and Rr (=$\Lambda^{1/2}\overline{Rt}\,\Lambda^{1/2}$), respectively. The complex correlation coefficient is determined by

utilizing the radiation pattern and is indicated by the off-diagonal (i, j) element of the matrix consisting of $\overline{Rr}$ and $\overline{Rt}$, whose diagonal elements are 1. The total efficiency of the ith port (η_{tot}) is represented by the ith element (i, i) of the diagonal matrix Λ [17].

3.4 MIMO CC: From the knowledge of SNR with the transmitting signal, the CC is calculated in 1 Hz of bandwidth using equation (5) from the H-matrix using equation (3) and equation (4) for both models. The CC is expressed as [17]:

$$CC = \log_2[\det(I_{nR} + \frac{SNR}{n_T}HH^*)] \qquad (5)$$

where det=determinant, SNR=average SNR, $I_{nR}=n_R \times n_R$ identity matrix, H = channel matrix, H*=Hermitian transpose, n_R =number of R_x antennas, and n_T =number of T_x antennas.

4. MIMO Capacity Results:

Further, the channel capacities are evaluated for channels created by $1T_x \times 1R_x$ using Ant. 1, $2T_x \times 2R_x$ using Ant. 2, $4T_x \times 4R_x$ using Ant. 3 with the matched loads connected to the remaining four ports, and $8T_x \times 8R_x$ using Ant. 3 based on both PLM and KM at 5 cm and 25 cm distances between T_x and R_x as shown in Table 3.

Table 3: Channel Details Used for CC Measurement

Name of channel	Type of Antenna used	No. of T_x antennas	No. of R_x antennas	Frequency used (GHz)	Distance (D) between T_x and R_x (cm)
Case 1	Ant. 1	1	1	2.1-2.8	5 and 25
Case 2	Ant. 2	2	2	3.1-4.0	5 and 25
Case 3	Ant. 3	4	4	3.1-4.0	5 and 25
Case 4	Ant. 3	8	8	3.1-4.0	5 and 25

The measured SNR of the channel formed in Case 1 is presented in Figure 4(a), which shows that the SNR values vary from 16.91dB to 18.38 dB. The measured SNR of the Case 2 and Case 3 are shown in Figure 4(b). The SNR values of Case 2 fluctuate from 26.78 to 29.36 dB and Case 3 varies from 27.27dB to 29.74 dB. The same SNR values are found for Case 4 as in Case 3.

As depicted in Figure 2(a), a pair of Ant. 1 is used to measure the path loss between them at 2.4 GHz. Figure 5 shows the (CC) obtained using PLM based on equations (2), (3) and (4) at two different distances of 5 cm and 25 cm. For both cases, the CC is less than 6 bps/Hz, which is low for the 4G networks whereas, the CC is approximately 3 bps/Hz at two different distances of 5 cm and 25 cm using KM (equations (4) and (5)) as considered only SNR.

The path loss between a pair of dual-polarized circular slot antennas is measured at 3.5 GHz as presented in Figure 2(b). Figure 6 shows the CC obtained from the PLM at 5 cm and 25 cm distances. When D= 5 cm, the CC is obtained from 32 to 34 bps/Hz. However, when D=25 cm, CC is achieved from 34 to 50 bps/Hz. The above data shows that for the frequency range of 3.5 GHz to 3.7 GHz, the CC shows the same kind of pattern for both distances. The CC obtained from the KM is increased from 5 to 13 bps/Hz at a 5 cm distance, while in the case of 25 cm, it fluctuates from 5 to 12 bps/Hz. The above data shows that for the operating band of 3.5 GHz for 5G, the channels can be transmitted with approximately the same CC for both distances.

An 8-port MIMO antenna as shown in Figure 2(c) is used in pairs to obtain the path loss between its various ports. To use as a 4-port antenna-based channel, the path loss between only the top 4-ports of this antenna is used to estimate the H-matrix. Figure 7 compares the CC from the PLM measurements at two different distances of 5 cm and 25 cm. In the case of 5 cm, the CC is obtained from 69 to 79 bps/Hz while in the case of 25 cm, CC fluctuates from 57 to 80 bps/Hz. For the frequency range of 3.5 GHz to 3.7 GHz, the CC shows a similar trend at both distances. When the number of antennas increases from 2 to 4,

there is a slight improvement in CC. In the case of 5 cm, the CC using KM is achieved from 13 to 20 bps/Hz. However, when D=25 cm, CC fluctuates from 5 to 20 bps/Hz.

(a)

(b)
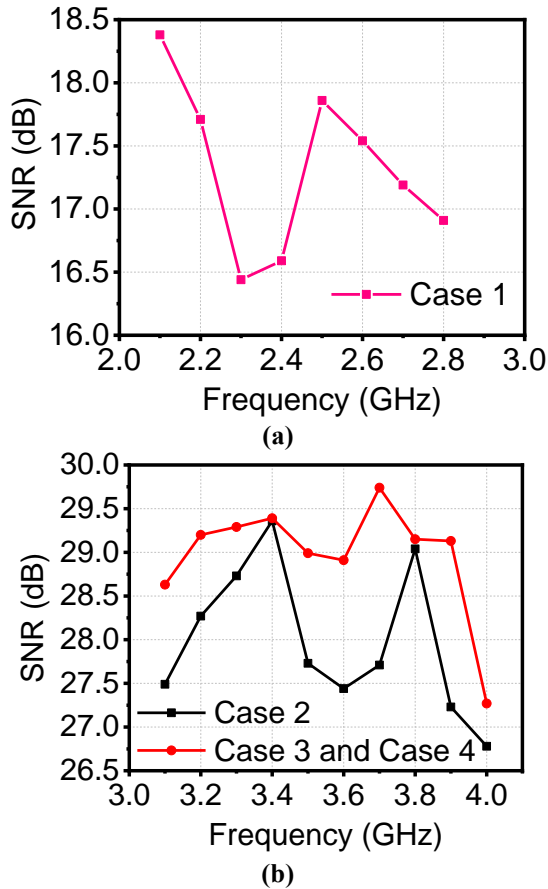
Figure 4: Measured SNR (a) Case 1, and (b) Case 2; Case 3 and Case 4.
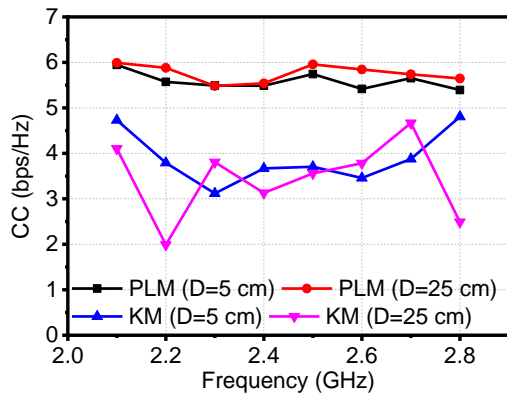
Figure 5: CC for Case 1 using PLM and KM.

Figure 8 shows the CC for channels formed using 8-ports of two identical MIMO antennas at two different distances of 5 cm and 25 cm obtained using PLM. The capacity growth varies from 137 bps/Hz to 157 bps/Hz for a 5 cm distance and from 94 bps/Hz to 135 bps/Hz for a 25 cm distance. In the 3.5 GHz to 3.7

GHz frequency band, the CC exhibits a comparable pattern at both distances. As a result, the CC significantly improves with the addition of eight antennas. Using the KM, the capacity growth varies from as low as 8 bps/Hz to a high value up to 36 bps/Hz in the case of 25 cm, and from 24 bps/Hz to 39 bps/Hz in the case of 5 cm. So, the CC shows a similar trend for both distances in most frequency points.
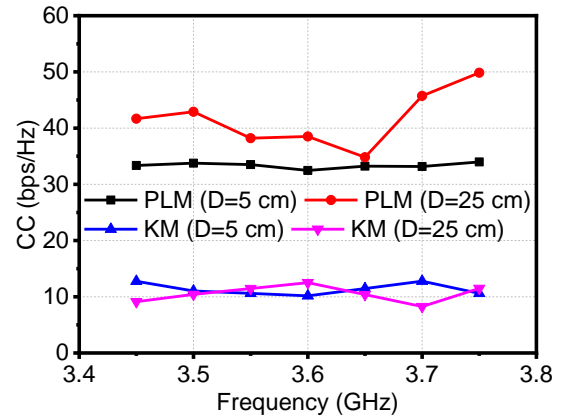
Figure 6: CC for Case 2 using PLM and KM.
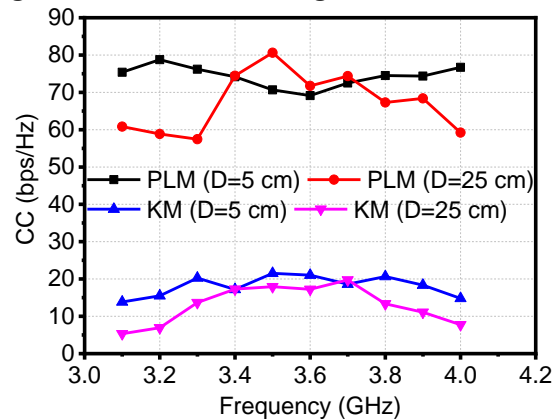
Figure 7: CC for Case 3 (4T×4R) using PLM and KM.

Figure 9 depicts the achievable channel capacities of all four cases at 3.5 GHz using PLM and KM for D=5 cm and 25 cm. It can be noted that the CC calculated using PLM is more than the KM. In Single Input Single Output (SISO) (Case 1), both PLM and KM provide almost the same CC. However, for MIMO Cases 2, 3, and 4, there is a significant difference in the CC. This is because in PLM, real transmission channels were considered which include SNR at both the transmitter's and receiver's end, and in KM, SNR only at the receiver is being considered and it takes care of

the total efficiency while the channel scenario is avoided.
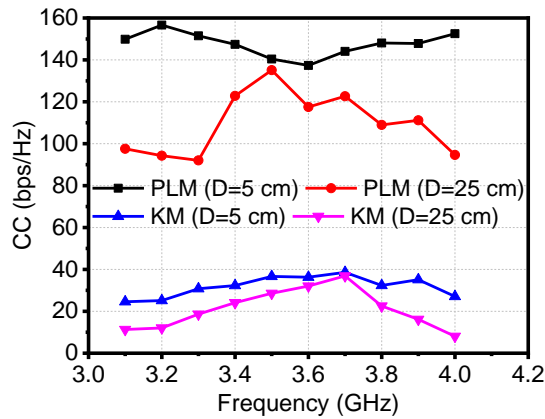
Figure 8: CC for Case 4 (8T×8R) using PLM and KM.
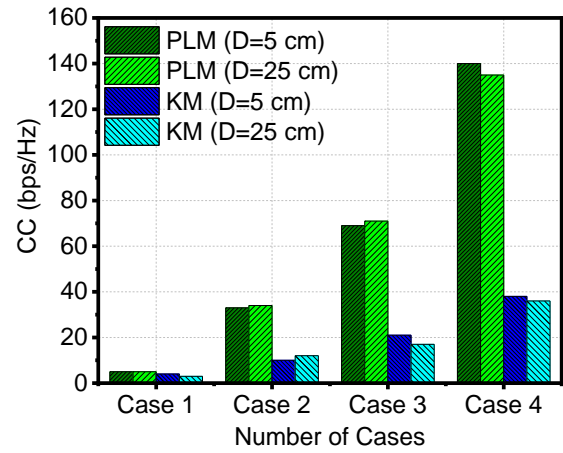
Figure 9: Comparison of channel capacities obtained for the four cases.

Table 4: Comparison of proposed work with other similar previously reported work

Ref.	No. of Antenna Elements	BW (GHz)	Isolation (dB)	Average SNR (dB)	Max. CC (bps/Hz)
[4]	4	2.4-2.44	>12	20 (Set value)	21
[5]	4	27.75-28.18/41.31-41.99	>20	20 (Set value)	21
[6]	4	2.42-7.45	>12	20 (Set value)	21.34
[7]	4	0.356–0.536	>20	20 (Set value)	19.9
[8]	12	3.4-3.6 (-6dB BW)	>10	20 (Set value)	59.87
[9]	2	2.45	NR	30 (Set value)	16
[18]	4	2.9-10.86	>22	NR	NR
[19]	4	3.1-10.6	>17	NR	NR
[20]	4	3.5-11	>17	NR	NR
[21]	4	2.3-13.75	>22	NR	NR
Case 1*	1	2.29-2.95	NA	17.35 (Measured)	PLM=5, KM=4
Case 2*	2	3.4-3.8	>16	28 (Measured)	PLM=34, KM=12
Case 3*	4	3.4-3.8	>15	29 (Measured)	PLM=71, KM=21
Case 4*	8	3.4-3.8	>15	29 (Measured)	PLM=140, KM=38

Note: * = This Work, BW=Bandwidth, and NR=Not Reported.

With the increase in the distance, no significant change in CC is observed for both PLM and KM. This shows that the CC is independent of the distance between T_x and R_x. As the number of T_x and R_x antennas increases, CC increases almost linearly in both PLM and KM. This confirms that the CC is dependent on the number of antennas on both the T_x and R_x sides. These results are important for using MIMO antennas in information and communication technology systems for the Smart City. So, the MIMO antenna with more number of antenna elements provides high data rates.

This work is finally compared with the recently reported work in Table 4, which has calculated CC. In the previous work [4]-[9], SNR is set to a fixed value of 20 dB or 30 dB, while other 4-port MIMO antennas are reported without CC [18]-[21]. None of the previously reported work has measured SNR and calculated CC using PLM and KM. Also, in the proposed work CC is calculated by varying the number of antennas at both T_x and R_x and keeping 5 cm and 25 cm distance between T_x and R_x antennas. Addressing the environmental challenges in outdoor networks faced by antennas used is critical for ensuring their long-term durability and reliability. Environmental factors such as temperature variation, humidity, precipitation, wind, dust, pollution, solar radiation, and atmospheric absorption can significantly impact channel performance in addition to multipath interference.

5. Conclusions: This paper investigates the Channel Capacity (CC) for WLAN and 5G bands at 2.4 GHz and 3.5 GHz bands, respectively, for different channels constructed utilising the 1-port, 2-port, 4-port, and 8-port antennas. Two models are used to evaluate the CC: path loss model (PLM) and Kronecker's model (KM). Because SNR just at the receiver is taken into account in KM, significant discrepancies in results are achieved when compared to those obtained by PLM. In path loss computation, however, genuine transmission channels were taken into account, which include SNR at both the transmitter and

receiver's end. Taking into account the impact on the CC in the many source scenarios makes the study valuable for wireless communication systems that use MIMO antennas.

Conflict of Interest:
Authors declare No conflicts of interest.

References:

[1] M. Qaraqe, Q. H. Abbasi, A. Alomainy and E. Serpedin, "Experimental Evaluation of MIMO Capacity for Ultrawideband Body-Centric Wireless Propagation Channels," *IEEE Antennas and Wireless Propagation Letters,* vol. 13, pp. 495-498, 2014.

[2] A. Ramachandran, S. Mathew, V. Rajan and V. Kesavath, "A Compact Tri band Quad-Element MIMO Antenna Using SRR Ring for High Isolation," *IEEE Antennas and Wireless Propagation Letters,* vol. 16, pp. 1409-1412, 2017.

[3] S. Ramasamy, and A. Madhu, "A Compact Tri-Band MIMO Antenna for WLAN and 5G Applications," *Applied Physics A,* vol. 130, p. 113, 2024.

[4] Y. S. Kim and D. -H. Cho, "Design of Four-Port Integrated Monopole Antenna Using Refraction Effect of Dielectric Medium for Pattern Gain Enhancement," *IEEE Antennas and Wireless Propagation Letters,* vol. 19, no. 4, pp. 621-625, April 2020.

[5] R. N. Tiwari, D. Sharma, P. Singh and P. Kumar, "Design of Dual-Band 4-Port Flexible MIMO Antenna for mm-Wave Technologies and Wearable Electronics," *IEEE Access,* vol. 12, pp. 96649-96659, 2024.

[6] S. K. Mahto, A. K. Singh, R. Sinha, M. Alibakhshikenari, S. Khan and G. Pau,

"High Isolated Four Element MIMO Antenna for ISM/LTE/5G (Sub-6GHz) Applications," *IEEE Access,* vol. 11, pp. 82946-82959, 2023.

[7] A. Iqbal, M. Al-Hasan, I. B. Mabrouk and M. Nedil, "Scalp-Implantable MIMO Antenna for High-Data-Rate Head Implants," *IEEE Antennas and Wireless Propagation Letters,* vol. 20, no. 12, pp. 2529-2533, Dec. 2021.

[8] B. Yang, Y. Xu, J. Tong, Y. Zhang, Y. Feng and Y. Hu, "Tri-Port Antenna With Shared Radiator and Self-Decoupling Characteristic for 5G Smartphone Application," *IEEE Transactions on Antennas and Propagation,* vol. 70, no. 6, pp. 4836-4841, June 2022.

[9] T. Xie et al., "Two-Way Power Divider With Wide Tunable Power Ratio Range for Weighted-Polarization MIMO Antenna in BAN Radios at 2.45 GHz," *IEEE Antennas and Wireless Propagation Letters,* vol. 21, no. 7, pp. 1333-1337, July 2022.

[10] P. Sehgal and K. Patel, "Performance Analysis and Impedance Modeling of Rectangular and Circular Split-Ring Resonator Antennas in 2.4/5.2 GHz Bands," *Progress In Electromagnetic Research C,* vol. 117, pp. 159-171, 2022.

[11] V. Kaushal, A. Birwal, and K. Patel, "Diversity characteristics of four-element ring slot-based MIMO antenna for sub-6-GHz applications," *ETRI Journal,* vol. 45, no. 4, pp. 581-593, 2023.

[12] V. Kaushal, A. Birwal, S. M. Patel, and K. Patel, "Diversified Path Loss Performance of Dual-Polarised MIMO Antenna in Sub-6 GHz for RFID Applications," *International Journal of Electronics,* vol. 111, no. 7, pp. 1196-1212, 2024.

[13] M. A. T. Alrubei, I. A. Alshimaysawe, A. N. Hassan, and A. H. K. Khawayyir, "Capacity Analysis and Performance Comparison of SISO, SIMO, MISO & MIMO Systems," in *Imam Al-Kadhum International Conference for Modern Applications of Information and Communication Technology*, Baghdad, Iraq, 2020.

[14] R. Ullah, S. Ullah, S.Faisal, I. B Mabrouk, M.J Al Hasan and B. Kamal, "A Novel Multi-Band and Multi-Generation (2G, 3G, 4G, and 5G) 9-Elements MIMO Antenna System for 5G Smartphone Applications," *Wireless Networks,* vol. 27, no. 7, pp. 4825-4837, 2021.

[15] V. Kaushal, A. Birwal, S. M. Patel and K. Patel, "Path Loss of Two-Port Circular-Ring Slot Antenna For RFID Applications," in *IEEE International Conference on RFID Technology and Applications (RFID-TA)*, Delhi, 2021.

[16] B. Holter, "On the Capacity of the MIMO Channel: A Tutorial Introduction," in *Int. Proc. IEEE Norwegian Symposium on Signal Processing*, Trondheim, 2001.

[17] B. Clerckx, and C. Oestges, "Analytical MIMO Channel Representations for System Design," in *MIMO Wireless Networks*, Academic Press, Dec. 2013, pp. 59-100.

[18] J. Zhang, C. Du, and R. Wang, "Design of a Four-Port Flexible UWB-MIMO Antenna with High Isolation for Wearable and IoT Applications," *Micromachines,* vol. 13, no. 12, p. 2141, 2022.

[19] T. Govindan, S. K. Palaniswamy, M. Kanagasabai, and S. Kumar, "Design and Analysis of UWB MIMO Antenna for Smart Fabric Communications," *International Journal of Antennas and Propagation,* vol. 2022, no. 1, p. 5307430, 2022.

[20] A. A. Ibrahim, M. I. Ahmed, and M. F. Ahmed, "A systematic investigation of four ports MIMO antenna depending on flexible material for UWB networks," *Scientific reports,* vol. 2022, p. 14351, 2022.

[21] Z. Tang, X. Wu, J. Zhan, S. Hu, Z. Xi and Y. Liu, "Compact UWB-MIMO Antenna With High Isolation and Triple Band-Notched Characteristics," *IEEE Access,* vol. 7, pp. 19856-19865, 2019.

Effect of Temperature on Electrochemical Behavior of Cobalt Diselenide Ternary Composite-based Supercapacitor

Shweta Tanwar[1], Nirbhay Singh[2], Anurag Gaur[1*], A.L Sharma[3*]

[1]*Department of Physics, Netaji Subhas University of Technology, Delhi-110078, India*

[2]*Department of Applied Physics, Amity School of Engineering and Technology, Amity University Gwalior Madhya Pradesh-474005, India*

[3]*Department of Physics, Central University of Punjab, Bathinda, Punjab-151401, India*

*Corresponding Author Email: anurag.gaur@nsut.ac.in; alsharma@cup.edu.in

Abstract: The electrochemical behavior of a cobalt diselenide ($CoSe_2$)-based ternary composite for hybrid supercapacitor applications across varying temperatures has been studied. To get advanced electrochemical results composite was synthesized by incorporating activated carbon and cellulose fibers with $CoSe_2$ (the optimization of the ternary composite is depicted in our other research paper). A series of electrochemical analyses was directed at different temperatures to assess the temperature-dependent behavior of the supercapacitor. The results demonstrate that the ternary composite exhibits enhanced electrochemical properties, with a high specific capacitance at 40°C temperatures due to improved ion mobility and charge transfer kinetics. At 40°C, the composite-based cell revealed a specific capacitance of 248 F g^{-1}, which further decreased at higher temperatures, showcasing a negative correlation between temperature and electrochemical performance. The energy and power densities obtained for the same are 22 Wh kg^{-1} and 411 W kg^{-1}. The findings suggest that such hybrid supercapacitors could play a dynamic part in energy storage technologies.

1. Introduction: The society is currently grappling with energy storage [1]. This situation is driven by several factors, including the limitations of renewable energy resources and the increasing energy demand due to population growth, among others. Conventional, energy sources (non-renewable) including fossil fuels are reducing speedily, prompting the scientific community to explore renewable energy as a sustainable alternative [2]. While renewable energy offers numerous advantages, it is not consistently reliable. However, this reliability can be improved through the development of energy storage devices. These devices help store energy generated from renewable sources, ensuring a steady supply during peak demand. Among the most common energy storage solutions are secondary batteries and supercapacitors [3]. Supercapacitors (SC), in particular, have gained popularity due to their benefits, including high reliability, cost-effectiveness, fast charge/discharge rates, excellent steadiness, high power density, and safety in use. Conventional supercapacitors are made of three main parts: a separator, electrolyte, and electrode [4]. Despite their advantages, supercapacitors face the disadvantage of low energy density of low value, which needs to be addressed in the future [5]. For

supercapacitors, the energy density is determined by its potential window and capacitance, as calculated using the formula $E = 0.5CV^2$ (Wh kg^{-1}) [6]. Both the potential window and capacitance hinge on the intrinsic assets of the electrode and electrolyte. Aqueous supercapacitors, based on their working machinery, are characterized as electric double-layer capacitors (EDLCs) and pseudocapacitors [7]. Hybrid SC, a third type, syndicates the profits of both EDLCs and pseudocapacitors while addressing issues such as low capacitance and energy density, and poor stability [8]. One way to improve the potential window is by designing electrode materials that can store charges through redox reactions. Electrode materials with unique morphologies, large surface areas, and favourable microstructures can significantly enhance a supercapacitor's capacitance [9].

Transition metal diselenides (MSe$_2$), where "M" can represent various transition metals have emerged as promising electrode materials for supercapacitors. Their popularity stems from characteristics like high area (surface), wide range oxidation states, low electronegativity, exceptional morphologies, and multifunctional electrical structures [10]. Commonly used MSe$_2$ compounds in supercapacitors include CoSe$_2$. For instance, Chen et al. synthesized a CoSe$_2$ electrode via a thermal method, achieving 554 F g^{-1} and a density (energy) of approximately 20 Wh kg^{-1} with a 1.7 V potential window [11]. However, pure CoSe$_2$ materials suffer from drawbacks such as low electronic conductivity, and limited capacitance. To overcome these limitations, researchers develop composite carbon-based materials. These carbon materials offer high surface area, admirable electronic conductivity, and boosted stability [12]. Notable studies in this area include Yu et al., who prepared a CoSe$_2$@carbon composite using a hydrothermal method, delivering 332 mF cm^{-2} capacitance and 95% cyclic stability [13]. Despite these improvements, binary

CoSe$_2$-carbon binary composites often experience agglomeration, complicating the electrolyte ion transport and insertion/extraction processes. To address this issue, the introduction of dispersants is needed to reduce aggregation, enhance electrolyte wettability, and shorten the dispersion path for ions of the electrolyte.

In this study, we assume that incorporating cellulose into cobalt diselenide composites can effectively reduce agglomeration, facilitate electron mobility by providing easy diffusion pathways, and improve electrochemical performance, particularly energy density and stability. Cellulose, being abundant, biocompatible, biodegradable, and mechanically stable, offers an improved surface area and abundant active locations, assembly it a perfect candidate for this role. To prevent clustering in CoSe$_2$-carbon nanocomposites we have utilized cellulose in this work. This paper presents the preparation of cellulose-incorporated ternary composites based on cobalt diselenides, using a room-temperature physical mixing approach (optimization of the ternary composite is depicted in our previous reports [1]). The objective of this study is to study the temperature effect on the electrochemical behavior of the designed supercapacitor based on a ternary composite of cobalt diselenide. Thus, the electrochemical behavior of the symmetric cell designed has been studied for various temperature ranges from 40 to 120°C.

2. Experimental Segment

2.1. Materials
The chemicals utilized for this study were procured from Sigma Aldrich as ACS-grade reagents and were used directly for synthesis without further purification. The materials include hydrazine hydrate (N$_2$H$_4$·H$_2$O), potassium hydroxide (KOH) pellets, Activated carbon (AC), selenium (Se) powder, polyvinylidene fluoride (PVDF), N-methyl-2-pyrrolidone (NMP), carbon black, and cobalt

nitrate hexahydrate (Co (NO₃)₂·6H₂O). Cellulose fiber (Sigma Aldrich, product number C6288) was used with a density of 0.600 g/cm³. The moisture content of the cellulose fiber was at least 10%. Double-distilled water (DDW) was used throughout the sample preparation process.

2.2 Synthesis of Cobalt diselenide ternary composite

The binary composites of CoSe₂, along with activated carbon (AC), were produced employing the hydrothermal technique as described in this report [14]. The ternary composites were prepared by physically blending the above-prepared binary composites with cellulose. Cellulose (weight percentage 5%), was incorporated into the binary composite matrix, and the blend was moved continuously for 6 hours. The resultant sample was dried in a controlled oven at 70°C for 12 hrs. The final samples were designated as CAC-40 for further analysis. The flowchart for the ternary composite preparation process is shown in **Fig. 1**. The reaction kinetics for the formation of the binary composites were detailed in one of our previous research articles [14]. The activated carbon coating on the pure CoSe₂ was designed to enhance stability and increase the area of the surface for pure CoSe₂.

2.3 Characterization tools used

X-ray diffraction (XRD) data was extracted by a PANalytical Empyrean diffractometer. The XRD curves were recorded over a 2θ range of 10 to 70 degrees. Fourier transform infrared (FTIR) spectra were attained by NEXUS-870

spectrometer, over 600-4000 cm⁻¹. The morphology was observed using a Merlin Compact system. The surface area cum pore size distribution was done by using the nitrogen adsorption-desorption technique with a BELSORP-maxII instrument (MicrotracBEL Corporation). The thermal steadiness of the manufactured sample was measured using thermogravimetric analysis (TGA) on a SHIMADZU DTG-60H instrument. The analysis was conducted under dynamic temperature ranging from 30°C to 550°C, in a nitrogen (N₂) atmosphere at 10°C/min (constant heating rate). Differential scanning calorimetry (DSC) was executed using a DSC-Sirius 3500 instrument from 30°C to 500°C, under a N₂ atmosphere at 10°C/min (sustained heating rate).

2.4 Electrochemical investigation

The electrodes of the organized composite material were fabricated by spread over a slurry paste onto a nickel (Ni) foam current collector, then dried at 60°C in an oven for several hours. The slurry was prepared by homogeneously mixing in a ratio of 80: 10: 10 (active material, PVDF binder, and carbon black (CB) in a solvent NMP. The mass of the active material was 3 mg coated on Ni foam (diameter of 1 cm). A symmetric cell was assembled to evaluate the electrochemical properties of the sample (prepared) in a two-electrode (2-E) system. The symmetric cell was created by placing a filter paper soaked in a few drops of 6 M KOH electrolyte between two identical electrodes. The assembled cell
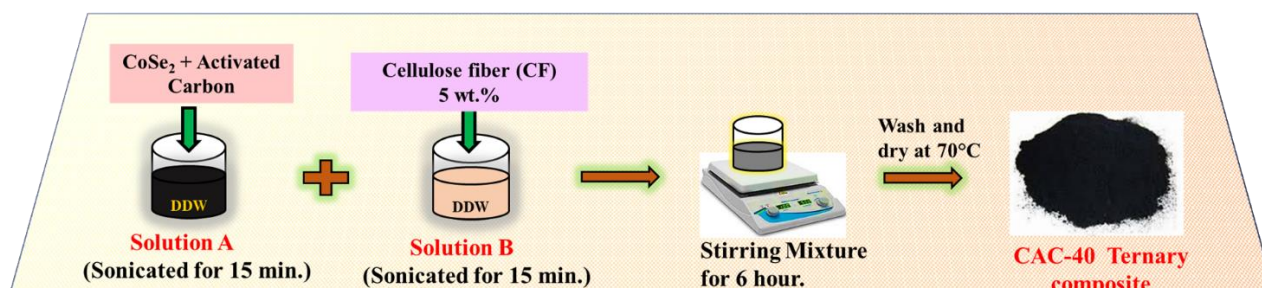

Figure 1. Schematic depiction of preparation of CoSe₂-based ternary composite.

can be represented symbolically as Electrode//Electrolyte//Electrode. The cell was further used for electrochemical testing.

The electrochemical analysis, like cyclic voltammetry (CV), galvanostatic charge-discharge (GCD), cum electrochemical impedance spectroscopy (EIS), was run on the symmetric cell via a 2-E (electrode) configuration. A CHI760E instrument was employed for these measurements. Whatman filter paper, with KOH (6M), was used as the separator. The use of a highly concentrated electrolyte was chosen due to the small size of OH⁻ ions, which results in high mobility and conductivity, thereby enhancing the electrochemical properties. CV and GCD readings were recorded over a potential range of -0.8 V to 0.8 V at varying scan rates and current densities. EIS data were taken across a frequency range of 1 Hz to 0.1 MHz, using a constant voltage of 5 mV. The following formulae were employed for calculating energy density, specific capacitance, and power density given below [15]:

Specific Capacitance

Using CV, $C_{S-CV} = \frac{\int iV\,dV}{m*v*\Delta V}$ (F g⁻¹)   (1)

GCD, $C_S = \frac{2*i*\int V\,dt}{m(\Delta V)^2}$ (F g⁻¹)   (2)

Energy density

From GCD, $E = \frac{C*V^2}{7.2}$ (Wh kg⁻¹)   (3)

and Power density

$P = \frac{E*3600}{t_d}$ (W kg⁻¹)   (4)

Here m, v, V, t_d, and I, are related to mass, scan rate, potential window, time of discharging, and current independently.

3. Results and discussion

3.1 Structural, Chemical, and Surface Analysis

The successful synthesis of the organized material was achieved through X-ray diffraction. **Fig. 2a** illustrates the XRD plot for pure AC, cobalt diselenide, cellulose, and the ternary composite (CAC-40). Cellulose fiber was merged into the binary composite which contains CoSe₂ and activated carbon (1:1). Additionally, 5% by weight of cellulose fiber was added to the binary composite of CoSe₂ and activated carbon. Two broad peaks at 25° and 43° correspond to crystalline planes of the activated carbon used. The (1$\bar{1}$0), (110), (200), and (004) planes connected to cellulose fiber show peaks at 15.1°, 16.2°, 22.7°, and 34.3°. In the XRD pattern for pure CoSe₂, peaks observed agree with the planes, matching the JCPDS card No. 053-0449. These peaks indicate the formation of the orthorhombic phase associated with CoSe₂, with lattice parameters 3.628 Å, 4.85 Å, and 5.827 Å [16]. The XRD pattern for sample CAC-40 authorizes the creation of the required composite.

The chemical atmosphere and validation of bonds cum groups in the synthesized ternary composite were investigated using the FTIR tool. **Fig. 2b** presents the FTIR bands for carbon, cellulose, cobalt diselenide, and prepared composite for 600 to 4000 cm⁻¹ wavenumber. The bands for ranges like 690-720 cm⁻¹ and 800–850 cm⁻¹ are accredited to O-Co-O vibrations cum Co-Se bonding [17]. Bands corresponding to C-O and C=O groups appeared at 1130 cum 1581 cm⁻¹. Peaks at 1050 cm⁻¹ and 1648 cm⁻¹ relating to C-O-C and -COO- stretching are for cellulose, while the -COO- band indicates the cellulose's electronegativity and dispersibility in water [18]. Peaks around 1539 cm⁻¹, cobalt (Co) complex. Bands around 2900 cm⁻¹ correspond to C-H functional groups in samples [19]. Broad peaks about 3000–3320 cm⁻¹ and 3350–3500 cm⁻¹ regions are credited to OH groups in the samples [1].

The surface area along with pore size for the composite samples was examined using isotherms methods (nitrogen adsorption-desorption). **Fig. 2c** illustrates the BET plot for

the prepared samples. The isotherm for the CAC-40 sample resembles a type-IV curve, indicating a mesoporous structure in the ternary composite. The pore size for this CAC-40 ranges from 0 to 160 nm. The N_2 adsorption/desorption scheme, along with the inset showing the pore size distribution arc for the CAC-40 sample, is presented in **Fig. 2c**. The area at the surface of CAC-40 was estimated to be 460 m² g⁻¹, with a pore diameter of around 4.1 nm. The BET results suggest that the CAC-40 ternary composite has a larger surface area, which could enhance the storage of the charges at both the outer and internal active sites. As a result, the CAC-40 sample is expected to demonstrate excellent electrochemical performance.

3.2 Temperature related studies

The stability with temperature variation of the CAC sample was verified through the Thermo-gravimetric analysis (TGA) tool. Initially, a weight reduction of approximately 2.6 % below 200 °C indicates the evaporation of moisture from the exterior area of the sample elements. Subsequently, a weight reduction of about 34.6 % is detected over the temperature range of 200 to 570 °C, reflecting the devolatilization of the material. As the TGA readings were conducted under an inert nitrogen atmosphere, the likelihood of oxidation or combustion of the constituents (such as cobalt, selenium, and carbon) in the sample is minimal. Consequently, we spot a
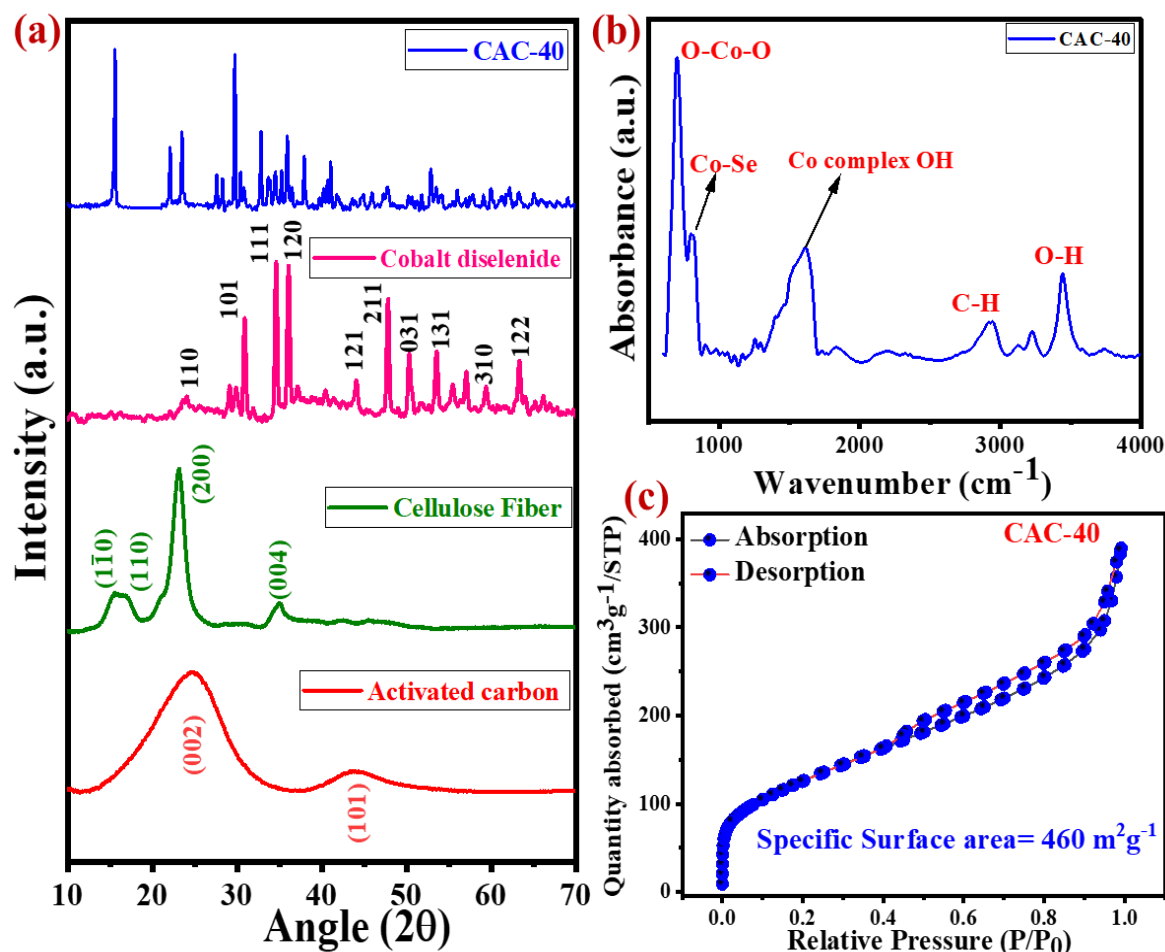

Figure 2. (a) X-ray diffraction, (b) FTIR plot, and (c) nitrogen adsorption-desorption isotherms for CAC-40 sample.

nonstop decay in the TGA curve through the complete temperature region.

DSC was employed to authorize the upsurge of conductivity (electrical) which is due to a growth of ions (free) and a reduction of crystallinity. **Fig.3b** shows the DSC results for the CAC-40 sample. The endothermic peak observed over the 0-300° C temperature range is accredited to the melting point of different components (selenium, carbon which is activated, and cellulose fiber) of the prepared composite. The exothermic peaks from 300-500° C temperature represent crystallization and the reaction of different components to formulate the ternary composite.

report outlined the rationale for coating $CoSe_2$ particles with activated carbon. The addition of cellulose fibers to the $CoSe_2$ and carbon composite was aimed at preventing the aggregation of $CoSe_2$ particles, creating a biodegradable and less contaminated material, and ensuring mechanical stability. This design optimizes the architecture of the composite to achieve a high area at the surface and a clear circulation path for ions associated with electrolytes, facilitating efficient charge storage.

3.4 Electrochemical investigation of the prepared cell for different temperature

The electrochemical properties of a composite made of $CoSe_2$ with cellulose were examined

Figure 3. (a) TGA, and (b) DSC for CAC-40 sample.

3.3 Morphology study via field emission scanning electron microscopy-FESEM

To explore the morphology of the ternary composite (CAC-40), we conducted an investigation using FESEM.

Fig.4 presents the FESEM pictures for the CAC-40 sample. The images reveal intact $CoSe_2$ particles enveloped by spherical activated carbon, with cellulose fibers visible throughout the structure. Additionally, the flakes of $CoSe_2$ are uniformly distributed and attached to the activated carbon. Our previous

using a 2-E configuration at 1.6 V (potential window) in a potassium hydroxide electrolyte of six molarity. The performance of the composite was evaluated through, GCD, EIS, and CV.
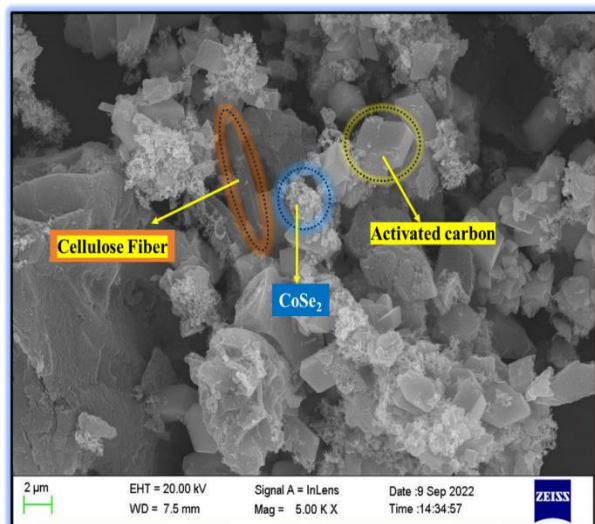
Figure 4. FESEM image for CAC-40 at 2 micrometers.

Fig. 5a presents the CV arcs of the ternary composite at dissimilar temperatures while measuring electrochemical measurements, ranging from 40°C to 120°C, with a 100-mV s⁻¹ scan rate. The CAC-40 material exhibited the largest CV curve area, indicating superior performance compared to other temperature-based samples. **Fig. 5b** shows the specific capacitance (Cs), estimated using equation 1, for all cells at various temperatures at a common scan rate. **Fig.5c** illustrates the CV curve for CAC-40 at different scan rates, revealing a distorted rectangular profile. This shape suggests that charge storage occurs
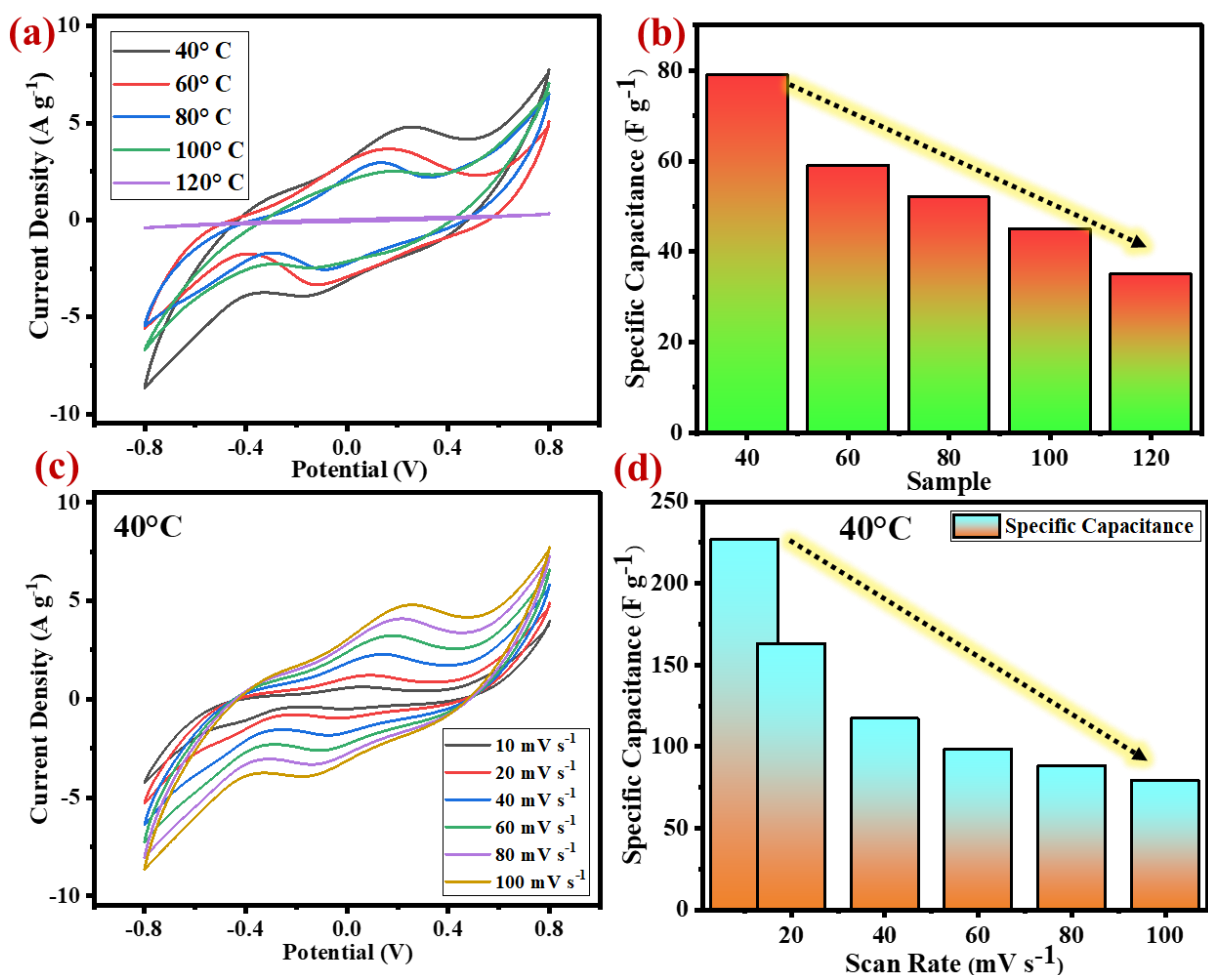
Figure 5. (a) CV plot for temperature range 40-120°C, (b) specific capacitance at 100 mV s⁻¹ for the sample at changed temperature ranges, (c) CV graph for CAC-40 at unlike scan rates, and (d) variation of capacitance with scan rate for CAC-40 sample.

through two processes: (1) the adsorption of electrolytic ions at the boundary of two components, creating an EDL at the boundary, and (2) a reversible faradaic process, involving the passage of electrolytic ions inner surface of the electrode material. **Fig. 5d** displays the specific capacitance (Cs) against the scan rate (10 to 100 mV s⁻¹). The Cs value declines with increasing scan rate, likely due to reduced ion accumulation on the electrode surface at higher scan rates.

Fig. 6a presents the GCD arcs for ternary composite samples synthesized at dissimilar temperatures, at 2 A g⁻¹. The GCD curve outline deviates from the typical convention shape for all samples at different temperatures, which is attributed to the contribution of mutually formed electrostatic layer and oxidation-reduction reactions, allowing for enhanced charge storage. **Fig. 6b** shows the

GCD profiles for CAC-40 at varying current densities.

The specific capacitance (C$_s$), calculated with equation 2 at unlike current densities (ranging from 1 to 5 A g⁻¹), is depicted in **Fig. 6c**. The drift in C$_s$ values obtained from GCD measurements aligns with the results of CV analysis across all samples. Electrochemical parameters for all samples at varied temperatures, calculated using equations 1 to 4, are summarized in **Table 1**. A Ragone plot proving the connection between power and energy density for CAC-40 is shown in **Fig. 6d.** The CAC-5 samples demonstrated the highest performance, delivering approximately 22 Wh kg⁻¹ (energy density) and power density of about 411 W kg⁻¹ for 1 A g⁻¹, outperforming other composite samples.
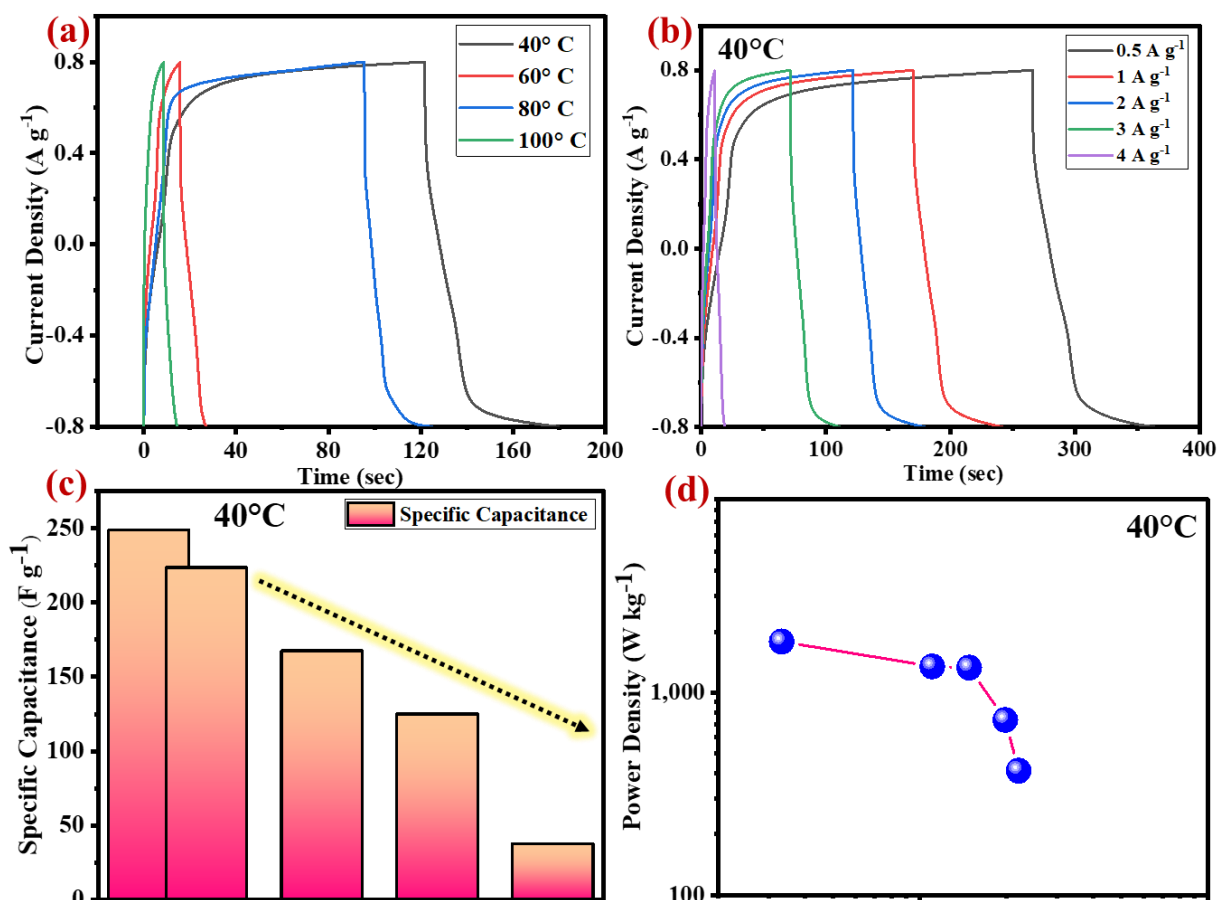

Figure 6. (a) GCD plot for the sample at unlike temperature (40-120°C), (b) GCD for CAC-40 at dissimilar current density, (c) specific capacitance change vs current density, and (d) Ragone graph for CAC-40 sample.

Table 1. Different electrochemical parameters for CAC-40 samples at different current densities

Current Densities (A g^{-1})	Specific Capacitance (F g^{-1})	Energy Density (Wh kg^{-1})	Power Density (W kg^{-1})
0.5	248	22	411
1	223	20	733
2	167	15	1329
3	125	11	1347
4	37	3	1786

The resistive and capacitive properties of the organized composites were investigated using EIS for frequency shifting from 0.1 Hz- 0.1 MHz. The Nyquist plots for all samples are revealed in **Fig. 7a**, highlighting two distinct frequency regions: (a) the high-frequency region, which exhibits a semicircle. The intersection of this semicircle with the X-axis, along with its diameter, represents the charge transfer resistance (R_{ct}) and bulk resistance; (b) the region of low-frequency, depicts a line that appears parallel to the Y-axis.

The bulk resistance (R_b) reflects the resistance within the cell, including interfaces and solvents. **Fig. 7b** presents a bar graph comparing the R_b and R_{ct} resistances of all samples at different temperatures. It reveals that the CAC-40 sample has the lowest bulk resistance ($R_b = 5.3 \ \Omega$) also $R_{ct} = 0.9 \ \Omega$ relative to other samples at varied temperatures. This low bulk resistance suggests that the CAC-40

material offers an efficient, unobstructed pathway for ion transport, promoting optimal charge storage.

In the proposed research, the functional properties of activated carbon will be thoroughly examined and incorporated to understand its impact on energy storage device performance. Activated carbon is widely recognized for its high surface area, excellent porosity, and stability, making it a valuable additive in energy storage systems, particularly for enhancing electrode performance. The study aims to explore how incorporating activated carbon into cobalt diselenide electrode materials can improve critical performance metrics such as electrochemical stability, energy density, and power density. Also, the incorporation of activated carbon and cellulose fibers significantly enhanced the electrochemical performance of the composite, resulting in a substantial increase in specific

Figure 7.(a) Nyquist plot, and (b) bar graph indicating bilk and charge transfer resistance for the cell at different temperatures.

capacitance and improved charge-discharge kinetics.

4. Conclusion

This study successfully demonstrates the electrochemical behavior of a cobalt diselenide ($CoSe_2$) --based ternary composite hybrid supercapacitor across varying temperatures. The electrode material depicted surface is about 460 m^2 g^{-1}. The incorporation of activated carbon and cellulose fibers significantly enhanced the electrochemical performance of the co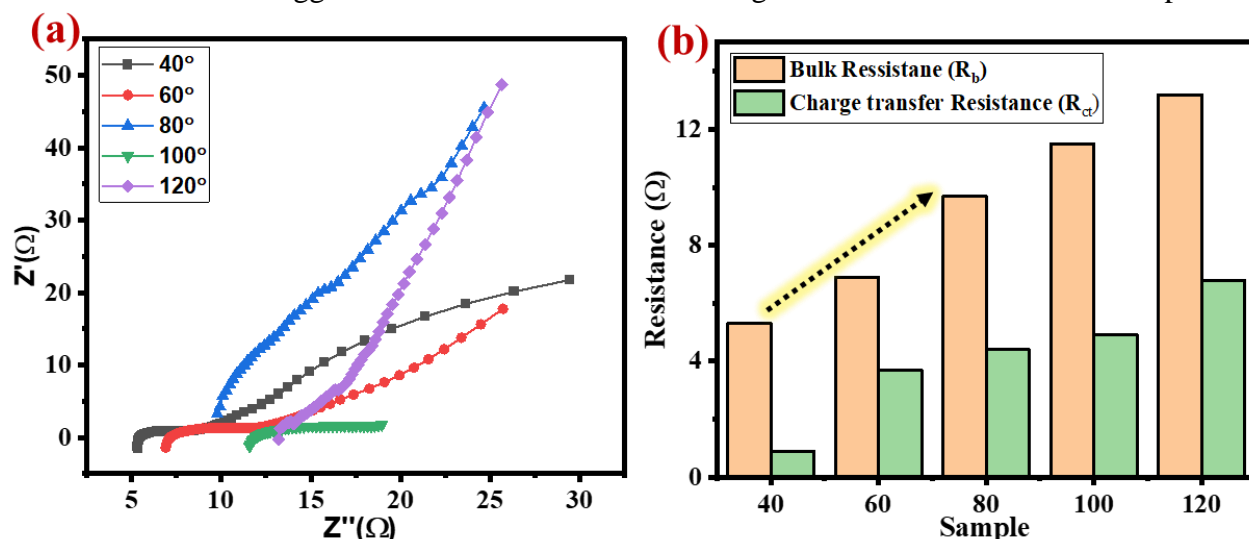mposite, resulting in a substantial increase in specific capacitance and improved charge-discharge kinetics. The composite-based cell at 40° C temperature revealed a specific capacitance of 248 F g^{-1}, which further decreased at higher temperatures, showcasing a negative correlation between temperature and electrochemical performance. The energy and power densities obtained for the same electrode are estimated at around 22 Wh kg^{-1} and 411 W kg^{-1}. Our findings reveal that the specific capacitance of the supercapacitor decreased with temperature, highlighting the negative impact of elevated temperatures on the ion's mobility and charge transfer efficiency. These results suggest that the ternary composite not only enhances energy storage capacity but also ensures reliable performance over extended use. Overall, the findings of this research indicate the promising potential of $CoSe_2$-based ternary composites for high-performance energy storage applications at around room temperature. Future research may focus on optimizing the composite's morphology and exploring additional synergistic materials to further enhance performance.

CReDiT authorship contribution statement

Shweta Tanwar: Conceptualization, Formal analysis, Investigation, Validation, Methodology, Visualization, Writing-Original draft, review, and editing. **Nirbhay Singh**-Investigation, Validation, Visualization, Writing- review, and editing. **Anurag Gaur**-Conceptualization, Visualization, Investigation, Supervision, Writing- review, and editing. **A. L. Sharma**: Visualization, Investigation, Writing-review, and editing, Supervision.

Declaration of Competing Interest

The authors declare that they have no known competing financial interests or personal relationships that could have appeared to influence the work reported in this paper.

References

[1]   Tanwar S, Singh N, Sharma AL. Cellulose-doped ternary composites for high-performance hybrid supercapacitor. Mater Res Bull 2024:113033.

[2]   Tanwar S, Sharma AL. Insight into use of biopolymer in hybrid electrode materials for supercapacitor applications—A critical review. J Appl Phys 2023;133.

[3]   Pateriya RV, Tanwar S, Sharma AL. Carbon decorated Li-based orthosilicate electrode for energy storage application. J Mater Sci 2024:1–18.

[4]   Tanwar S, Arya A, Gaur A, Sharma AL. Transition metal dichalcogenide (TMDs) electrodes for supercapacitors: a comprehensive review. J Phys Condens Matter 2021;33:303002. https://doi.org/10.1088/1361-648x/abfb3c.

[5]   Tanwar S, Singh N, Kour S, Sharma AL. Investigation of temperature effect on the electrochemical performance of MoSe2@ FeOOH composite. AIP Conf. Proc., vol. 2995,

AIP Publishing; 2024.

[6]   Singh N, Tanwar S, Sreehari MS, Sharma AL, Yadav BC. An approach to substitute costly-commercial capattery electrodes by activated carbon@ Co with advanced retention: Detailed device study supported by DFT investigation. J Energy Storage 2024;80:110244.

[7]   Kour S, Tanwar S, Singh N, Sharma AL. Electrochemical performance of ZnCo2O4 nanosheets in aqueous electrolytes for supercapacitor applications. AIP Conf. Proc., vol. 2995, AIP Publishing; 2024.

[8]   Sarathi MTV, Tanwar S, Sreehari MS, Mondal K, Sharma AL. Surfactants effect on the electrochemical properties of FeSe2 electrode for supercapacitor with first principles insights into quantum capacitance. Ceram Int 2024;50:7266–80.

[9]   Singh N, Tanwar S, Kumar P, Sharma AL, Yadav BC. Advanced sustainable solid state energy storage devices based on FeOOH nanorod loaded carbon@ PANI electrode: GCD cycling and TEM correlation. J Alloys Compd 2023;947:169580.

[10]   Tanwar S, Singh N, Vijayan AK, Sharma AL. Electrochemical performance investigation of different shaped transition metal diselenide materials based symmetric supercapacitor with theoretical investigation. Surfaces and Interfaces 2023;42:103504.

[11]   Chen T, Li S, Gui P, Wen J, Fu X, Fang G. Bifunctional bamboo-like CoSe2 arrays for high-performance asymmetric supercapacitor and electrocatalytic oxygen evolution. Nanotechnology 2018;29:205401.

[12]   Singh N, Tanwar S, Sharma AL, Yadav BC. Economic and environment friendly carbon decorated electrode for efficient energy storage devices. J Energy Storage 2023;66:107452.

[13]   Yu N, Zhu M-Q, Chen D. Flexible all-solid-state asymmetric supercapacitors with three-dimensional CoSe 2/carbon cloth electrodes. J Mater Chem A 2015;3:7910–8.

[14]   Tanwar S, Singh N, Sharma AL. Fabrication of Activated Carbon coated MSe2 (M= Mo, Co, and Ni) Nanocomposite Electrode for High-Performance Aqueous Asymmetric Supercapacitor. Colloids Surfaces A Physicochem Eng Asp 2023:131235.

[15]   Tanwar S, Singh N, Sharma AL. Structural and electrochemical performance of carbon coated molybdenum selenide nanocomposite for supercapacitor applications. J Energy Storage 2022;45:103797.

[16]   Tanwar S, Singh N, Sharma AL. High-performance different shape carbon decorated asteroidea-like cobalt diselenide electrode for energy storage device. Fuel 2022;330:125602. https://doi.org/https://doi.org/10.1016/j.fuel.2022.125602.

[17]   Ariponnammal S, Velvizhi R. Structural, EPR, magnetic and photoluminescence studies on cobalt selenide. Invertis J Sci Technol 2016;9:1–5.

[18]   Mojoudi N, Mirghaffari N, Soleimani M, Shariatmadari H, Belver C, Bedia J. Phenol adsorption on high microporous activated carbons prepared from oily sludge: equilibrium, kinetic and thermodynamic studies. Sci Rep 2019;9:1–12.

[19]   Manigandan R, Giribabu K, Suresh R, Vijayalakshmi L, Stephen A, Narayanan V. Cobalt oxide nanoparticles: characterization and its electrocatalytic activity towards nitrobenzene. Chem Sci Trans 2013;2:S47–50.

Performance of the AlGaN/GaN HEMT with Sunken Source Connected Field Plate under High Voltage Reverse Bias Step Stress

Chanchal[1]*, Amit Malik[2], Robert Laishram[2], D. S. Rawal[2], and Manoj Saxena[3]

[1]*Department of Electronic Science, University of Delhi, Delhi, India*
[2]*Solid State Physics Laboratory, Defence Research & Development Organization, Delhi, India*
[3]*Department of Electronics, Deen Dayal Upadhyaya College, University of Delhi, Delhi, India*

*Correspondence Author Email: chanchal0210saraswat@gmail.com

Abstract: The manuscript investigates the DC performance of conventional HEMT and Sunken Source Connected Field Plate (SSC-FP) HEMT reliability under reverse bias step stress. To assess the electrical performance of the device at the gate terminal is subjected to a high reverse bias step stress up to – 40 V with an increase of – 5 V step. A higher degree of ON–state resistance (R_{ON}) degradation is observed in the conventional HEMT than in the SSC-FP HEMT device. Post-stress drain to source current (I_{ds}) degradation is ~11% and ~6% in non-FP and with SSC-FP devices respectively. In conventional devices when gate voltage (V_{GS}) is up to -20V, the device leakage current is recoverable but after that, the gate current increases exponentially and becomes noisy. In SSC-FP devices, this behavior is shown after gate voltage -30V.

Keywords: AlGaN/GaN HEMT, Threshold Voltage Shift, OFF–State Stress, Reliability.

1

Introduction: The birth of AlGaN/GaN High Electron Mobility Transistors (HEMTs) represent a significant breakthrough in the field of semiconductor technology, particularly for applications requiring high power, high frequency, and high-temperature operation [1-4]. These devices exploit the unique properties of Gallium Nitride (GaN), a wide-bandgap semiconductor, and the AlGaN/GaN heterojunction to achieve superior performance compared to traditional silicon-based transistors [5, 6]. GaN's wide bandgap of 3.4 eV allows for higher breakdown voltages, greater power density, and improved thermal stability, making it an ideal choice for demanding environments such as radar systems, satellite communications, and power electronics [7, 8]. New applications in 5G communication infrastructure, electric vehicles, and renewable energy systems are emerging as key areas where these devices could drive transformative technological advancements [9-12]. Moreover, the integration of AlGaN/GaN HEMTs with other semiconductor technologies, such as silicon carbide (SiC) and diamond, holds promise for further enhancing the power handling capacity and efficiency of these devices [10].

The structure of AlGaN/GaN HEMTs is particularly noteworthy for its ability to generate a high-density two-dimensional electron gas (2DEG) at the heterojunction interface [11]. This 2DEG, formed without doping, enables extremely high electron mobility, leading to low on-resistance and fast switching speeds. As a result, AlGaN/GaN HEMTs have rapidly gained traction in the defense, telecommunications, and automotive industries, where performance and efficiency are paramount [12-14].

Looking toward the future, ongoing research into AlGaN/GaN HEMT devices is expected to unlock even more advanced capabilities. Efforts are focused on improving device reliability, thermal management, and scalability for mass production. However, improving their reliability under high operating voltage conditions remain a critical challenge. The introduction of a Sunken

Source Connected Field Plate (SSC-FP) in AlGaN/GaN HEMTs has proven to be an effective solution that enhances device performance and reliability [13, 14]. This design has a metal plate parallel to the gate terminal and is connected to the source through the mesa region, significantly reduces the parasitic capacitances (C_{gs} and C_{gd}) compared to other field plate technology. SSC-FP suppresses electric field peaks at the gate edge towards the drain terminal, and improves the breakdown voltage, which is crucial for high-power applications such as X-band radar systems and power amplifiers in satellite communications [10-12]. The future research will likely focus on further optimizing this structure for better thermal management and scalability, ensuring that AlGaN/GaN HEMTs remain a keystone of high-power electronics.

A study by Bothe *et al.,* demonstrated that HEMTs with an SSC-FP exhibit over 10 W/mm saturated output power and superior reliability, with an estimated lifetime exceeding 6×10^7 hours at 225°C, a more than two-fold increase over conventional designs [14]. Also, Zhu *et al*. reported that FP helps mitigate the detrimental effects of the inverse piezoelectric effect and trapping phenomena, which are often exacerbated under reverse-bias stress conditions [15]. This work investigates the performance of non-FP and SSC-FP HEMT devices under high reverse bias step stress.

The article is structured as follows: Section 2 presents the details of the device structure and fabrication process. Section 3 compiles the DC IV measurements and reliability studies and summarizes them with extracted parameters. Finally, the manuscript concluded in Section 4.

2. Experimental Methodology: AlGaN/GaN HEMTs were grown on SiC substrates using metal-organic chemical vapor deposition technique, with 25nm thick $Al_{0.25}Ga_{0.75}N$ on a 2μm semi-insulating GaN buffer. Standard Ti/Al/Ni/Au source/drain ohmic contact metallization is done using the e-beam evaporation technique and annealed at 820 °C

for 30 sec. Device isolation is carried out using the nitrogen implantation process. T-shaped Ni/Au gate contact were fabricated using slit etching. Devices were passivated using 100nm SiN_x deposited by plasma-enhanced CVD [13]. HEMTs with gate length, source-drain spacing, gate-drain spacing, and gate width of 0.4, 6, 4.6, and 100 μm, respectively. Schematic of the non-FP and with SSC-FP is shown in Fig.1 (a & b). The process flow of the fabrication of the devices is shown in Fig. 2. The measurement procedure is shown in Fig. 3, the fabricated devices were subjected to OFF state step stress at room temperature. Electrical measurements were carried out using Semiconductor Parametric Analyzer SCS-4200A.
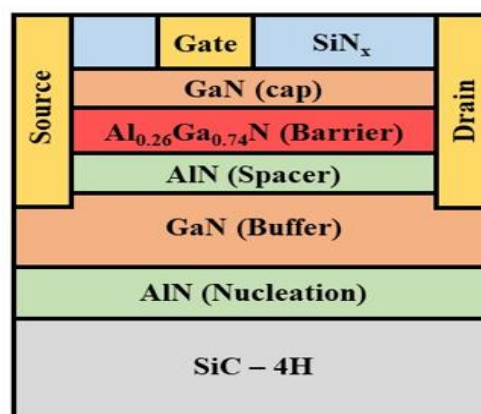
(a)
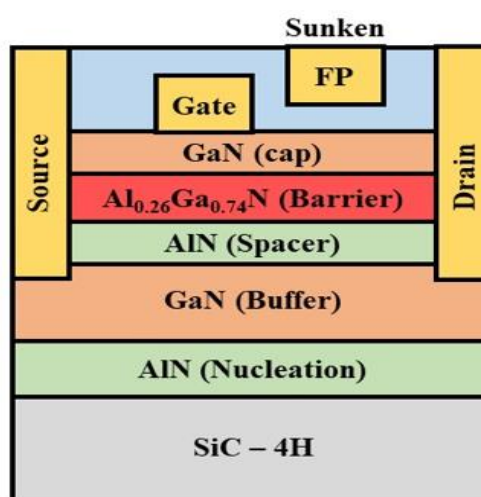
(b)

Figure 1. (a) and, (b) Schematic representations of the conventional (non-FP) and the SSC-FP HEMT device, respectively.
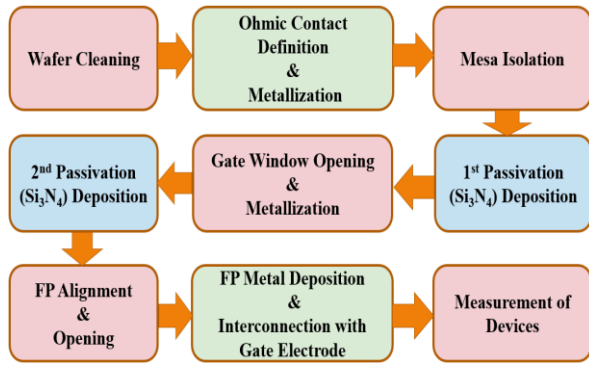
Figure 2. Flow chart of the fabrication of AlGaN/GaN HEMT devices.
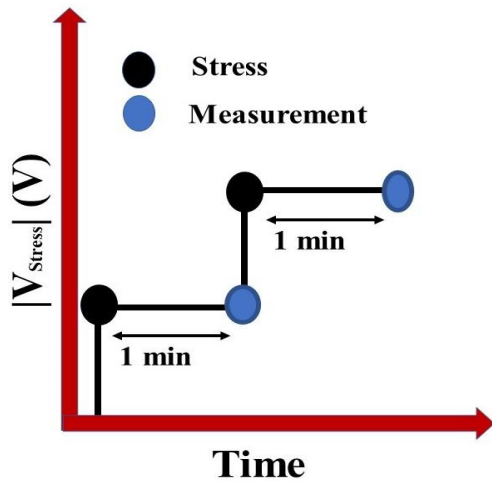
Figure 3. Shows the measurement procedure of the device.

As shown in Fig. 3, device pre-measurement is carried out and then the gate reverse bias is increased with the step of -5V. Devices were subjected to 60 second stress cycles, and electrical measurements were taken after each stage.

3. Results & Discussions:

3.1 Two Terminal Schottky Diode measurements: Forward and reverse Characteristics of the Schottky is carried out, as shown in Fig. 4 (a & b). The Φ_B and η are calculated using the thermionic emission (TE) model by using the standard diode equations (1) and (2):

$$I = I_S \left[\exp \left(\frac{qV - IRD}{\eta kT} \right) - 1 \right] \quad (1)$$

$$I_S = AA^*T^2 \exp \left(-q\,\Phi_B / kT \right) \quad (2)$$

where,

q= carrier charge,

k= Boltzmann's constant,
T= Temperature,
Φ_B= Schottky barrier height
η = Ideality factor,
A= Diode area,
I_S= Reverse saturation current
IR_D = Voltage drop across the diode, and
A*= Richardson constant for AlGaN.

Table 1 summarizes the extracted parameters before and after stress.
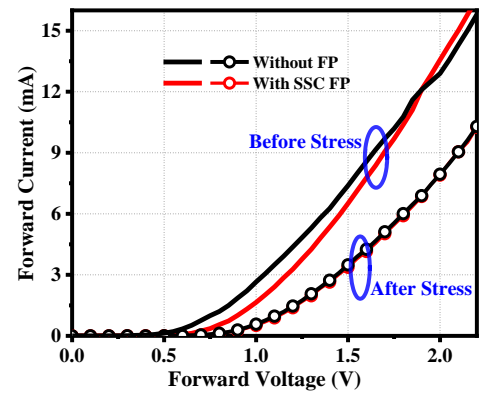
(a)
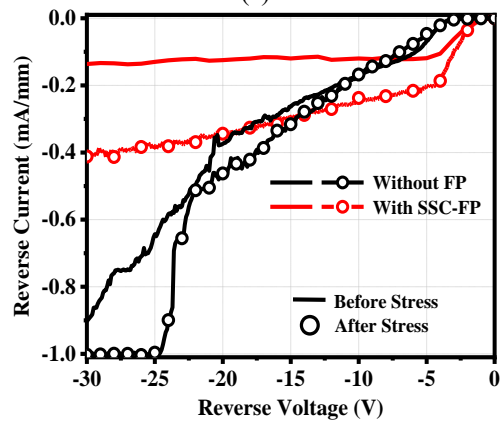
(b)

Figure 4. Comparison of (a) Forward, and (b) Reverse two terminal Gate characteristics of Non-FP and SSC-FP HEMT devices after step stress (V_g=-40V).

Table 1 Comparison of two terminal (Schottky Parameters) of the Non-FP and SSC-FP HEMT devices.

Device	Diode Parameters			
	Before stress		After stress	
	Φ_B (eV)	η	Φ_B (eV)	η
Without FP	0.910	1.15	0.856	1.56
With SSC-FP	0.905	1.16	0.867	1.47

As Fig. 4 shows the degradation in the Schottky parameters after step stress. The continuous stress at the gate (Ni/Au) leads to Nickel diffusion and corresponds to the degradation of the gate edge [17].

3.2 Three Terminal Device Measurements:

• **Reverse Bias Step Stress at the Gate Terminal:** In the step stress measurement technique, stress is applied incrementally overtime at the gate terminal. In this experiment, the V_{GS} was stepped by -5V. The device's leakage current was measured for 60 seconds at each step stress. The results of high reverse bias gate voltage step stress are shown in Fig. 5. The findings suggest that leakage remains recoverable up to a gate voltage of -20V and -30V, in conventional and SSC-FP devices respectively, which attributed to the trapping of electrons beneath the gate region. In non-FP devices at V_{gs} =-20V, the gate current becomes noisy and undergoes a significant increase, signaling the degradation in device performance while in the SSC-FP device, it is observed after V_{gs}=-30V.

As high voltage is applied to the gate terminal, the vertical electric field in the device increases which induces leakage paths in silicon nitride and AlGaN barrier which causes a rise in the gate current [17, 18]. Also, it is described that a high electric field deteriorates the original lattice parameters of the barrier layer and induces an inverse piezoelectric phenomenon [16]. Also, Zanoni *et al*. [18] reported through electroluminescence (EL) studies that hot-spot formation at the gate edge under high reverse bias contributes to the rise in leakage current. DC characterization is carried out before and after each step of stress to observe the current collapse phenomenon, which manifests in the form of an increase in the dynamic resistance (R_{ON}) of the device. Fig. 5 (a & b) shows the increase in the R_{ON}, V_{TH} shift, and increase in off-state leakage current post-stress in both non-FP and FP devices. Post stress a reduction in drain transconductance (g_D) and gate

transconductance (g_M) is also observed as shown in Fig. 5 (a) and Fig. 5 (c) respectively. Degradation in gate contact and defects generation can be observed with the increase in gate leakage current which is shown in Fig. 5(d) with time. Table 2, explains the change in the parameters post-step stress.

(a)

(b)

(c)
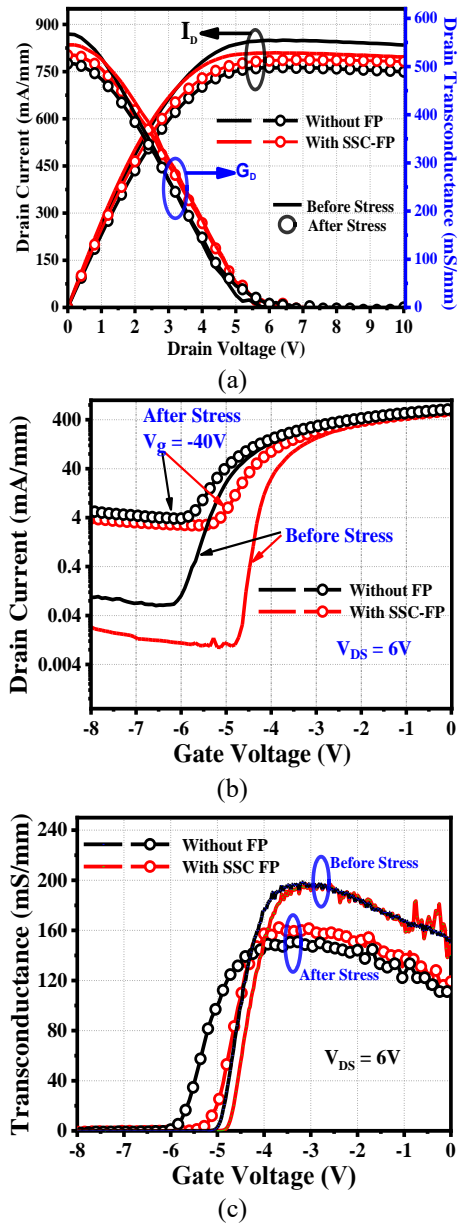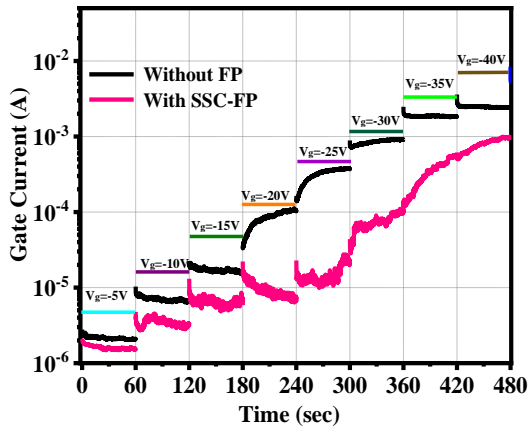
(d)

Figure 5. Post reverse bias step stress scheme, (a) Output characteristics, (b) & (c) shows transfer characteristics, and (d) gate current as a function of transient time.

Table 2 summarizes the change in device parameters before and post-stress.

Parameters		Device	
		Without FP	With SSC-FP
I_{DS} (mA/mm)	Before Stress	850	830
	After Stress	760	778
	Δ (%)	10.6	6.3
R_{ON} (Ω·mm)	Before Stress	4.56	4.55
	After Stress	6.25	5.02
	Δ (%)	37.0	10.3
V_{TH} (V)	Before Stress	-4.98	-4.85
	After Stress	-5.82	-5.25
	Δ (%)	16.8	8.24
G_m	Before Stress	190	190
	After Stress	148	160
	Δ (%)	22.1	15.8

Here, delta (Δ) represents the change in the parameters. A remarkable degradation is observed in the conventional HEMT as compared to the SSC-FP HEMT devices.

4. Conclusions: A comparative study of conventional HEMT and SSC-FP HEMT devices is studied. Post reverse bias step stress, the electrical performance of the device is investigated. Conventional devices are more vulnerable to degradation under high electric fields compared to SSC-FP HEMT devices. The SSC-FP device reduces the peak of the vertical electric field which prevents the degradation of the device parameters like threshold voltage (V_{TH}) shift and R_{ON}. Post reverse bias step stress up to -40V, the degradation of ~11% and 37% in I_{DS} and R_{ON}, respectively in the case of the conventional device against the ~6% and ~10% degradation recorded in the SSC-FP HEMT device the I_{DS} and R_{ON}, respectively. The SSC-FP design introduces several reliability benefits under high reverse-bias step stress. The reduction in the electric field intensity near the gate edge leads to a lower likelihood of premature device failure, which is particularly critical when operating at high drain-source voltages.

CRedit Author Statement
Chanchal: Conceptualization, Methodology, Visualization, Data analysis and interpretation, Investigation and Writing – Original Draft.
Amit Malik: Visualization, Reviewing and Editing Supervision, Technical Inputs.
Robert Laishram: Technical Inputs and Proofreading.
Dipendra Singh Rawal: Supervision, Writing- Reviewing and Editing, Validation, Technical Inputs and Resources.
Manoj Saxena: Supervision, Proofreading, Writing- Reviewing and Editing, Technical Inputs.

Conflict of Interest: Authors declare No conflicts of interest.

5. References:

[1]   S. Krause *et al.*, AlScN/GaN HEMTs Grown by Metal-Organic Chemical Vapor Deposition With 8.4 W/mm Output Power and 48 % Power-Added Efficiency at 30 GHz, IEEE Electron Device Letters, vol. 44, no. 1, pp.   17-20,   Jan.   2023.   DOI: 10.1109/LED.2022.3220877.

[2]   N. Collaert *et al.*, III-V/III-N technologies for next generation high - capacity   wireless   communication, International Electron Devices Meeting (IEDM), San Francisco, CA, USA, 2022, pp. 11.5.1-11.5.4.   DOI: 10.1109/IEDM45625.2022. 10019555.

[3]   P. Wang *et al.*, Evaluation of Power and Linearity at 30 GHz in AlGaN/GaN HEMT Fabricated by Integrating Transistors with Multiple Threshold Voltages, IEEE Transactions on Electron Devices, vol. 71, no. 3, pp. 1421-1427, March 2024. DOI: 10.1109/TED.2023.3347710.

[4]   A. Hickman *et al.*, 2.2 W/mm at 94 GHz in AlN/GaN/AlN High Electron Mobility Transistors on SiC, Physica Status Solidi A, vol. 220, no. 16, January 2023. DOI: 10.1002/pssa.202200774.

[5]   A. S. Razeen *et al.*, Structural, optical, and   electrical   characterization   and performance comparison of AlGaN/GaN HEMT structures with different buffer layers, Vacuum, Vol. 219, art. no. 112704, January 2024. DOI: 10.1016/j.vacuum.2023.112704.

[6]   D. Y. Chen *et al.*, Impact of the Channel Thickness on Electron Confinement in MOCVD-Grown High Breakdown Buffer-Free AlGaN/GaN Heterostructure, Physica Status Solidi A, Vol. 220, no. 16, art. no. 2200496,   September   2022.   DOI: 10.1002/pssa.202200496.

[7]   N Islam *et al.*, Reliability, Applications and Challenges of GaN HEMT Technology for Modern Power Devices: A Review, Crystals, Vol. 12, Issue 11, 2022. DOI: 10.3390/cryst12111581.

[8]   A. K. Visvkarma *et al.*, Comparative study of Au and Ni/Au gated AlGaN/GaN high electron mobility transistors, AIP Advances, vol. 9, no. 12, art. no. 12531, December 2019. DOI: 10.1063/1.5116356.

[9]   D. M. Fleetwood, X. Li, E. X. Zhang, R. D. Schrimpf and S. T. Pantelides, Low-Frequency Noise Due to Iron Impurity Centers in GaN-Based HEMTs, IEEE Transactions on Electron Devices, vol. 71, no. 2, pp. 1024-1030, Feb. 2024, doi: 10.1109/TED.2023.3347212.

[10]   Nicholas C. Miller *et al.*, A Survey of GaN HEMT Technologies for Millimeter-Wave Low Noise Applications, Vol. 3, IEEE Journal   of   Microwaves,   2023.   DOI: 10.1109/JMW.2023.3313111.

[11]   X. Ding *et al.*, Gate leakage mechanisms of the AlGaN/GaN HEMT with fluorinated graphene passivation, Materials Science in Semiconductor Processing, vol. 162, art. no. 107502, August 2023. DOI: 10.1016/j.mssp.2023. 107502.

[12]   Wei-Min Wu *et al.*, ESD Failures of GaN-on-Si D-Mode AlGaN/GaN MIS-HEMT   and   HEMT   Devices   for   5G Telecommunications,   2021   43rd   Annual EOS/ESD Symposium (EOS/ESD), Tucson, AZ,   USA,   2021,   pp.   1-7.   DOI: 10.23919/EOS/ESD52038.2021.9574716.

[13]   Chanchal *et al.*, Physical insights into the reliability of sunken source connected field plate GaN HEMTs for mm-wave applications, Volume   148,   115170, Microelectronics Reliability (2023). DOI: 10.1016/j.microrel.2023.115170.

[14]   K. Bothe *et al.*, Improved X-Band Performance and Reliability of a GaN HEMT with Sunken Source Connected Field Plate

Design, IEEE Electron Device Letters, March 2022. DOI: 10.1109/led.2022.3146194.

[15]   Q. Zhu *et al.,* Investigation of Inverse Piezoelectric Effect and Trap Effect in AlGaN/GaN HEMTs under Reverse-Bias Step Stress at Cryogenic Temperature, IEEE Access   (2020).   DOI: 10.1109/ACCESS.2020.2975118.

[16]   K Mazumdar *et al.,* Nanocrack formation due to inverse piezoelectric effect in AlGaN/GaN HEMT, Superlattices and Microstructures, Vol. 125, Pages 120-124,2019.DOI: 10.1016/j.spmi.2018.04.038.

[17]   J. A. del Alamo, and Jungwoo Joh., GaN   HEMT   reliability. Microelectronics reliability 49, no. 9-11 (2009): 1200-1206. https://doi.org/10.1016/j.microrel.2009.07.003.

[18]   Enrico Zonani *et al.,* Localized damage in AlGaN/GaN HEMTs induced by reverse-bias testing. IEEE Electron Device Letters 30, no. 5 (2009): 427-429. https://doi.org/10.1109/LED.2009.2016440.

Numerical Approximation Methods and Comparison with RK-4 Method for a Linear Differential Equation with Initial Conditions Using Scilab 6.1.1

Ravindra Singh[1*], Omwati Rana[2], Yogesh Kumar Sharma[3], Shiv Shankar Gaur[1]

[1]*Department of Physics, Shivaji College (University of Delhi), Raja Garden New Delhi-110027.*
[2]*Department of Physics, Daulat Ram College (University of Delhi), Maurice Nagar, New Delhi-110007.*
[3]*Department of Chemistry, Kalindi College (University of Delhi), East Patel Nagar New Delhi-110008.*

*Corresponding Author Email: ravindrasingh@shivaji.du.ac.in

Abstract: Numerical approximation methods have been developed to linear differential equation with initial condition. The comparison of the results has been done among Euler's method, modified Euler's method and RK-4 with the help of Scilab software 6.1.1. RK-4 method is effective enough to reach more accuracy in the result. The Runge-Kutta method attempts to overcome the problem of the Euler's method, and modified Euler's method and the study shows that in all cases RK-4 method improves to a great extent, than those by the Euler method and Modified Euler's Method. For RK-4 the approximation accuracy is proportional to the fourth power of the step size, thus making it a powerful and widely used numerical method also this method gives us higher accuracy without performing more calculations. Three different values of the step size have been taken. It is observed that smaller values of step size give better result; in all cases RK-4 method fits best as compared to others. The nature of the plot obtained by directly matches with the approximation solutions. It is observed that RK-4 method is suitable for obtaining the accurate solution of ODEs when the taken step sizes are too much small; since smaller h reduces the error.

Keywords: Ordinary Differential Equation, Initial Conditions, Step size, Accuracy Analysis, Absolute Error and Scilab software 6.1.1.

1. Introduction: Scilab is a free and open-source, cross-platform with highly numerical calculation package. It has multiple uses and wide applications in all branch of sciences and engineering. Numerical methods are techniques by which mathematical problems are formulated so that they can be analyzed with arithmetic operations although there are many kinds of numerical methods, they have one common characteristic: they invariably involve large numbers of tedious arithmetic calculations. To solve differential equations we have many methods but in this paper we have opted only three method named Euler's method, modified Euler's method and RK-4 method. Operations with ODE having significant role when it was done through scilab, the programming starts with the detailed modeling an ODE with three different styles [1]. In a comparison of performance of the CP scheme, Polygon, Harmonic-Polygon, and Cube-Polygon schemes it was found that all enhance Euler methods. The CP scheme achieves higher accuracy while requiring less computing time when applied to the RCL circuit equation for second-order ODE [2]. A System of non-homogeneous equations using matrix exponential method was studied and analyzed using Scilab software 6.1.1 [3]. All the results obtained by ODEs with initial conditions can be analyzed with the help of softwares and then the results

compared. These days Scilab software so popular, we used it in this paper (Scilab software 6.1.2 with window operating system). Result Analysis with accuracy at given initial conditions for ODEs done by M. A. Arefin at.el. using modified Euler method [4]. A demonstration study done on RK-4 method by using MATLAB Programming [5]. The numerical solutions for Euler's method and RK4 for ordinary differential equations (ODEs) were solved using Scilab [6]. Multiple numerical solutions to intuitionistic fuzzy differential equations have been studied as well as the traffic flow problem using RK4 method and [7-9]. Many times the linear differential equations of second order with different ways and different methods had been compared by Runge-Kutta methods [10-12]. Numerical methods such as RK4 etc. are commonly used for solving mathematical problems that are formulated in science and engineering where it is difficult or even impossible to obtain exact solutions these methods use mathematical modelling forms an important part of many tertiary courses in mathematics and engineering. Numerical methods provide a vehicle for you to reinforce your understanding of mathematics. RK-4 methods is to reduce higher mathematics to basic arithmetic operations it is a rich collection of numerical algorithms covering many aspects of scientific computing problems such as ordinary differential equations which can solve by Matlab also [13]. Non-linear partial differential equations such as a specific fluid flow problem can be easily solved by RK-4 method as well as it is capable solve a complex problem, physically or geometrically. The Various methods such as RK-4 and numerical techniques the basic fundamentals for the differential equations as well as mathematical modelling and engineering problem done by S. C. Chapra, R. P. Canale and D. Houcque [14-16]. The short list of its capabilities for matrices, polynomials, linear equation, signal processing, ODE's for numerical methods always involve with the topics related to generate the matrices which are solving the linear equation, ordinary differential equation (ODE's) and numerical integration [17-18].

IMPORTANCE & APPLICATIONS OF RK-4 METHOD

RK-4 METHOD: Runge Kutta was not a single person but two names collectively and the Runge Kutta method was named after these two German mathematicians-Carl David Tolmé Runge and Wilhelm Kutta. Runge Kutta method is an iterative method, where the successive approximations are generated to reach the final result and each iteration requires function evaluations at several points within the step interval. This method can be used for 'n' iterations to solve the differential equation; in this method the approximation accuracy is proportional to the fourth power of the step size, thus making it a powerful and widely used numerical method.

RK-4 is called **fourth-order Runge-Kutta method** for approximating the solution to the problem with initial value $y' = f(x, y)$ with initial condition $y(x_0) = y_0$ at the points
$x_{n+1} = x_0 + nh$ in an interval with slope as an arithmetic average
where n = 0, 1,2,3 . . .

$$\mathbf{y_{n+1} = y_n + \frac{1}{6}(k1 + 2k2 + 2k3 + k4);}$$

where
$k_1 = hf(x_0, y_0)$
$k_2 = hf\left(x_0 + \frac{h}{2}, y_0 + \frac{k_1}{2}\right)$
$k_3 = hf\left(x_0 + \frac{h}{2}, y_0 + \frac{k_2}{2}\right)$
$k_4 = hf(x_0 + h, y_0 + k)$

Applications:
1. It controls the accuracy and adjustment of the step size.
2. It suited very well to solve linear and non-linear initial value fuzzy problems.
3. It can be used to solve a complex problem, physically or geometrically.

4. It us higher accuracy without performing more calculations.

5. It is also used to solve both higher order ordinary differential equations and coupled (simultaneous) differential equations.

6. It can be used to solve non-linear partial differential equations such as a specific fluid flow problem.

7. It gives more accurate result as compared to above two methods. The solution curves were infact generated using a Runge-Kutta approximation.

8.We can take different value of step size, h.

SCILAB PROGRAMMING/CODING FOR EULER'S METHOD:

```
funcprot(0);
function dy=f(x, y)
dy=y-x;
endfunction
C=1;
x0=0;        //initial value of x
y0=1/2;  //initial value of y
h=0.1;    //step size It can be 0.01;0.05 etc
xn=1;
n=(xn-x0)/h;  //no. of steps
x=zeros(n+1,1)
y=zeros(n+1,1)
x(1)=x0;
y(1)=y0;
disp('x      y        Exact Soln  Abs Error');
for i=1:n
   x(i+1)=x(i)+h;
y(i+1)=y(i)+h*f(x(i),y(i))
end
yexact=C+x-(1/2)*exp(x);  //it is an exact
soln after solving DE manually
plot(x,y,':r',x,yexact,'--b','linewidth',2)
//plots
xlabel('x→','fontsize',6)
ylabel('y↑','fontsize',6,'rot',0)
title('h=0.1','fontsize',4)
legend('Euler Solution','Exact Solution',2)
error=yexact-y;
a=yexact-y;
abs(a);
disp([x,y,yexact,abs(a)])
```

SCILAB PROGRAMMING/CODING FOR EULER'S MODIFIED METHOD:

```
funcprot(0);
function dy=f(x, y)
dy=y-x;
endfunction
x0=0;//initial value of x
y0=1/2;//initial value of y
h=0.1;//step size It can be 0.01;0.05 etc
xn=1;
n=(xn-x0)/h;
x=zeros(n+1,1)
y=zeros(n+1,1)
x(1)=x0;
y(1)=y0;
disp('x      y        Exact Soln  Abs Error');
for i=1:n
   x(i+1)=x(i)+h;
yc(i+1)=y(i)+h*f(x(i),y(i))
y(i+1)=y(i)+0.5*h*(f(x(i),y(i))+f(x(i+1),yc(i+1)))
end
yexact=1+x-(1/2)*exp(x);//it is the exact
soln after solving DE manually
plot(x,y,':r',x,yexact,'--b','linewidth',2)
xlabel('x→','fontsize',6)
ylabel('y↑','fontsize',6,'rot',0)
title('h=0.05','fontsize',4)
legend('Eulers Modified','Exact Solution',2)
error=yexact-y;
a=yexact-y;
abs(a);
disp([x,y,yexact,abs(a)])
```

SCILAB PROGRAMMING/CODING FOR RK-4 METHOD:

```
funcprot(0);
function dy=f(x, y)
   dy=y-x;
endfunction
x0=0;
y0=1/2;
h=0.1; //step size It can be 0.01;0.05 etc
n=(xn-x0)/h; //no. of steps
x=zeros(n+1,1)
y=zeros(n+1,1)
x(1)=x0;
y(1)=y0;
```

```
disp('x      y       Exact Soln  Abs Error');
for i=1:n;
x(i+1)=x(i)+h;
k1=h*f(x(i),y(i));
k2=h*f(x(i)+h/2,y(i)+k1/2);
k3=h*f(x(i)+h/2,y(i)+k2/2);
k4=h*f(x(i)+h,y(i)+k3);
y(i+1)=y(i)+(1/6)*(k1+2*k2+2*k3+k4);
end
yexact=(1+x)-(1/2)*exp(x);//it is the exact
soln after solving DE manually
plot(x,y,':r',x,yexact,'--b','linewidth',2)
xlabel('x→','fontsize',6)
ylabel('y↑','fontsize',6,'rot',0)
title('h=0.05','fontsize',4)
legend('RK4','Exact Solution',2)
error=yexact-y;
a=yexact-y;
abs(a);
disp([x,y,yexact,abs(a)])
```

Ordinay method:
```
clc
clf
funcprot(0);
function dy=f(x, y)
    dy = y-x
endfunction
x0 = 0;
y0 = 1/2;
x=0:0.01:1;
y=ode(y0,x0,x,f)
plot(x,y,'linewidth',2)
xlabel('x→','fontsize',6)
ylabel('y↑','fontsize',6,'rot',0)
```
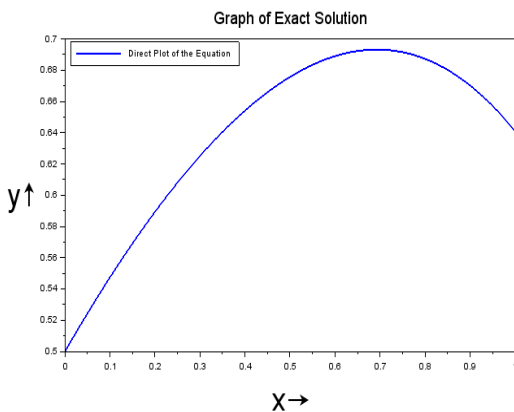

Figure 1. Solution by direct method

```
title('Graph of Exact Solution','fontsize',4)
legend('Direct Plot of the Equation',2)
```

Now continuing with a systematic manner, we generate the approximations listed in Tables 1-3 where we have rounded the calculations to seven decimal places.

Table 1. [Figure 2(a)-2(c)] Approximate solution for different step sizes with exact solution and absolute value.

| x	y	Exact Solution	Abs Error
EULER			
h=0.1			
0.	0.5	0.5	0.
0.1	0.55	0.5474145	0.0025855
0.2	0.595	0.5892986	0.0057014
0.3	0.6345	0.6250706	0.0094294
0.4	**0.66795**	**0.6540877**	**0.0138623**
0.5	0.694745	0.6756394	0.0191056
0.6	0.7142195	0.6889406	0.0252789
0.7	0.7256415	0.6931236	0.0325178
0.8	0.7282056	0.6872295	0.0409761
0.9	0.7210262	0.6701984	0.0508277
1.	0.7031288	0.6408591	0.0622697
Euler's Modified			
0.	0.5	0.5	0.
0.1	0.5475	0.5474145	0.0000855
0.2	0.5894875	0.5892986	0.0001889
0.3	0.6253837	0.6250706	0.0003131
0.4	**0.654549**	**0.6540877**	**0.0004613**
0.5	0.6762766	0.6756394	0.0006373
0.6	0.6897857	0.6889406	0.0008451
0.7	0.6942132	0.6931236	0.0010895
0.8	0.6886055	0.6872295	0.001376
0.9	0.6719091	0.6701984	0.0017107
1.	0.6429596	0.6408591	0.0021005
RK-4			
0.	0.5	0.5	0.
0.1	0.5474146	0.5474145	4.237D-08
0.2	0.5892987	0.5892986	9.365D-08
0.3	0.6250708	0.6250706	0.0000002
0.4	**0.6540879**	**0.6540877**	**0.0000002**
0.5	0.6756397	0.6756394	0.0000003
0.6	0.688941	0.6889406	0.0000004
0.7	0.6931242	0.6931236	0.0000005
0.8	0.6872302	0.6872295	0.0000007
0.9	0.6701993	0.6701984	0.0000008
1.	0.6408601	0.6408591	0.000001
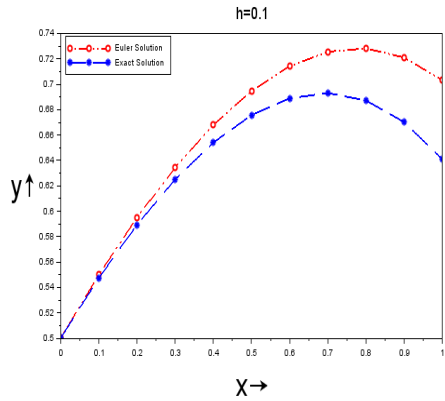
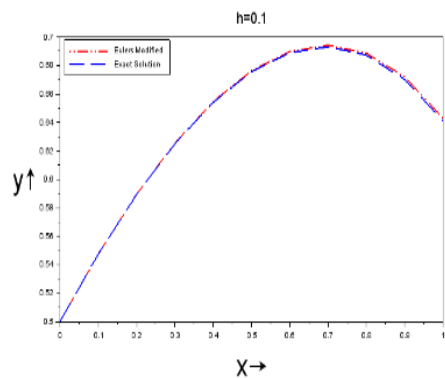**Figure 2(a). Approximate curve for step size h=0.1**

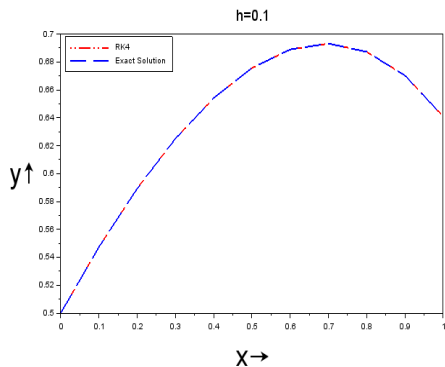**Figure 2(b). Approximate curve for step size h=0.1**

Figure 2(c). Approximate curve for step size h=0.1

Table 2. [Figure 3(a)-3(c)] Approximate solution for different step sizes with exact solution and absolute value

| EULER			
h=0.05			
x	y	Exact Solution	Abs Error
0.05	0.525	0.5243645	0.0006355
0.1	0.54875	0.5474145	0.0013355
0.15	0.5711875	0.5690829	0.0021046
0.2	0.5922469	0.5892986	0.0029483
0.25	0.6118592	0.6079873	0.0038719
0.3	0.6299522	0.6250706	0.0048816
0.35	0.6464498	0.6404662	0.0059836
0.4	**0.6612723**	**0.6540877**	**0.0071846**
0.45	0.6743359	0.6658439	0.008492
0.5	0.6855527	0.6756394	0.0099133
0.55	0.6948303	0.6833735	0.0114568
0.6	0.7020718	0.6889406	0.0131312
0.65	0.7071754	0.6922296	0.0149458
0.7	0.7100342	0.6931236	0.0169106
0.75	0.7105359	0.6915	0.0190359
0.8	0.7085627	0.6872295	0.0213332
0.85	0.7039908	0.6801766	0.0238143
0.9	0.6966904	0.6701984	0.0264919
0.95	0.6865249	0.6571452	0.0293797
1.	0.6733511	0.6408591	0.0324921
Euler's Modified			
0.	0.5	0.5	0.
0.05	0.524375	0.5243645	0.0000105
0.1	0.5474367	0.5474145	0.0000222
0.15	0.5691179	0.5690829	0.000035
0.2	0.5893476	0.5892986	0.000049
0.25	0.6080517	0.6079873	0.0000644
0.3	0.6251519	0.6250706	0.0000813
0.35	0.6405659	0.6404662	0.0000997
0.4	**0.6542074**	**0.6540877**	**0.0001197**
0.45	0.6659855	0.6658439	0.0001416
0.5	0.6758048	0.6756394	0.0001654
0.55	0.6835648	0.6833735	0.0001913
0.6	0.68916	0.6889406	0.0002194
0.65	0.6924794	0.6922296	0.0002498
0.7	0.6934065	0.6931236	0.0002828
0.75	0.6918186	0.6915	0.0003186
0.8	0.6875868	0.6872295	0.0003572
0.85	0.6805756	0.6801766	0.000399
0.9	0.6706426	0.6701984	0.0004441
0.95	0.657638	0.6571452	0.0004929
1.	0.6414045	0.6408591	0.0005454
RK-4			
0.	0.5	0.5	0.
0.05	0.5243645	0.5243645	1.313D-09
0.1	0.5474145	0.5474145	2.761D-09
0.15	0.5690829	0.5690829	4.353D-09
0.2	0.5892986	0.5892986	6.102D-09
0.25	0.6079873	0.6079873	8.019D-09
0.3	0.6250706	0.6250706	1.012D-08
0.35	0.6404662	0.6404662	1.241D-08
0.4	**0.6540877**	**0.6540877**	**1.491D-08**
0.45	0.6658439	0.6658439	1.763D-08
0.5	0.6756394	0.6756394	2.059D-08
0.55	0.6833735	0.6833735	2.381D-08
0.6	0.6889406	0.6889406	2.731D-08
0.65	0.6922296	0.6922296	3.110D-08
0.7	0.6931237	0.6931236	3.521D-08
0.75	0.6915	0.6915	3.966D-08
0.8	0.6872296	0.6872295	4.447D-08
0.85	0.6801766	0.6801766	4.968D-08
0.9	0.6701985	0.6701984	5.530D-08
0.95	0.6571452	0.6571452	6.136D-08
1.	0.6408592	0.6408591	6.790D-08
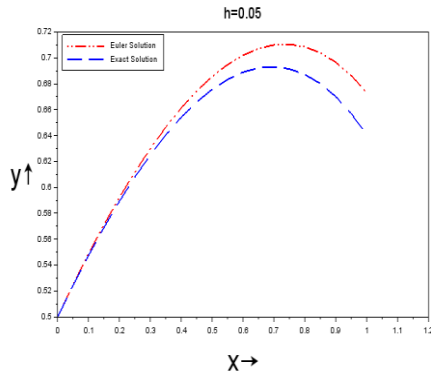
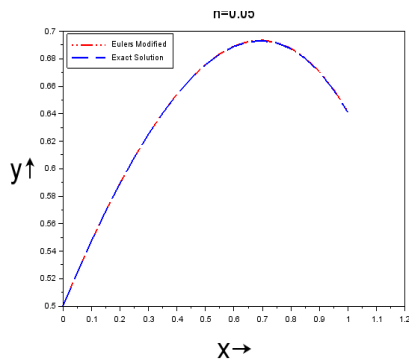**Figure 3(a). Approximate curve for step size h=0.0.5**

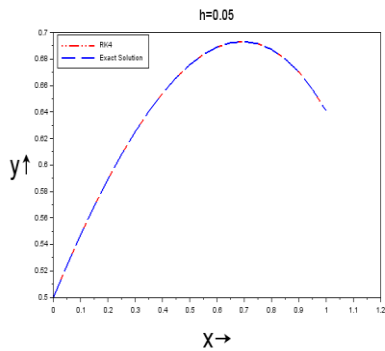**Figure 3(b). Approximate curve for step size h=0.05**

Figure 3(c). Approximate curve for step size h=0.05

Table 3. [Figure 4(a)-4(c)] Approximate solution for different step sizes with exact solution and absolute value

| EULER			
h=0.01			
x	y	Exact Solution	Abs Error
0.	0.5	0.5	0.
0.01	0.505	0.5049749	0.0000251
0.02	0.50995	0.5098993	0.0000507
0.03	0.5148495	0.5147727	0.0000768
0.04	0.519698	0.5195946	0.0001034
0.05	0.524495	0.5243645	0.0001305
0.06	0.5292399	0.5290817	0.0001582
0.07	0.5339323	0.5337459	0.0001864
0.08	0.5385716	0.5383565	0.0002152
0.09	0.5431574	0.5429129	0.0002445
0.1	0.5476889	0.5474145	0.0002744
0.2	0.589905	0.5892986	0.0006064
0.3	0.6260755	0.6250706	0.0010049
0.4	**0.6555681**	**0.6540877**	**0.0014805**
0.5	0.6776841	0.6756394	0.0020447
0.6	0.6916517	0.6889406	0.0027111
0.7	0.6966183	0.6931236	0.0034947
0.8	0.6916424	0.6872295	0.0044129
0.9	0.6756837	0.6701984	0.0054852
1.	0.6475931	0.6408591	0.006734
Euler's Modified			
0.	0.5	0.5	0.
0.05	0.524375	0.5243645	0.0000105
0.1	0.5474367	0.5474145	0.0000222
0.15	0.5691179	0.5690829	0.000035
0.2	0.5893476	0.5892986	0.000049
0.25	0.6080517	0.6079873	0.0000644
0.3	0.6251519	0.6250706	0.0000813
0.35	0.6405659	0.6404662	0.0000997
0.4	**0.6542074**	**0.6540877**	**0.0001197**
0.45	0.6659855	0.6658439	0.0001416
0.5	0.6758048	0.6756394	0.0001654
0.55	0.6835648	0.6833735	0.0001913
0.6	0.68916	0.6889406	0.0002194
0.65	0.6924794	0.6922296	0.0002498
0.7	0.6934065	0.6931236	0.0002828
0.75	0.6918186	0.6915	0.0003186
0.8	0.6875868	0.6872295	0.0003572
0.85	0.6805756	0.6801766	0.000399
0.9	0.6706426	0.6701984	0.0004441
0.95	0.657638	0.6571452	0.0004929
1.	0.6414045	0.6408591	0.0005454
RK-4			
0.	0.5	0.5	0.
0.01	0.5049749	0.5049749	4.174D-13
0.02	0.5098993	0.5098993	8.431D-13
0.03	0.5147727	0.5147727	1.277D-12
0.04	0.5195946	0.5195946	1.720D-12
0.05	0.5243645	0.5243645	2.172D-12
0.06	0.5290817	0.5290817	2.633D-12
0.07	0.5337459	0.5337459	3.102D-12
0.08	0.5383565	0.5383565	3.581D-12
0.09	0.5429129	0.5429129	4.069D-12
0.1	0.5474145	0.5474145	4.567D-12
0.2	0.5892986	0.5892986	1.009D-11
0.3	0.6250706	0.6250706	1.673D-11
0.4	**0.6540877**	**0.6540877**	**2.466D-11**
0.5	0.6756394	0.6756394	3.406D-11
0.6	0.6889406	0.6889406	4.518D-11
0.7	0.6931236	0.6931236	5.825D-11
0.8	0.6872295	0.6872295	7.357D-11
0.9	0.6701984	0.6701984	9.147D-11
1.	0.6408591	0.6408591	1.123D-10
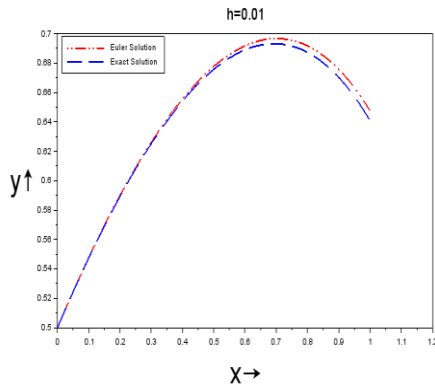
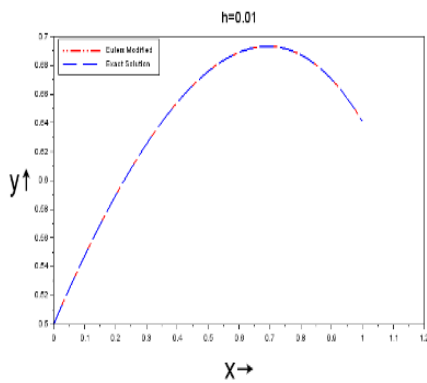**Figure 4(a): Approximate curve for step size h=0.0.1**

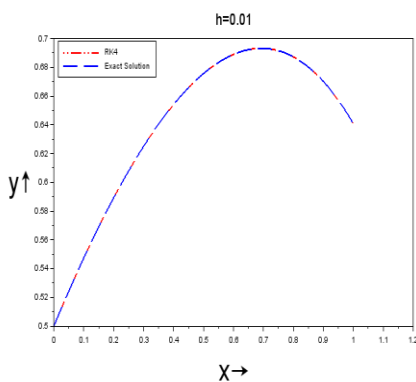**Figure 4(b). Approximate curve for step size h=0.01**

Figure 4(c). Approximate curve for step size h=0.01

3. Result Analysis: The programming has been done through Scilab and the codes successfully run. All the graphs have been plotted with the help of software at different values of step size, h=0.1, 0.05 and 0.01 for Euler's method, Euler's modified method

and RK-4 method respectively. The few properties like line, marker, style, fontsize, title, labes, linewidth, rotation and legend etc. have been used in the graph for betterment of the figures. The obtained resulting values are displayed in tabulated form for above three method and their comparison. For h=0.1 it is observed that there is some error in the result for Euler's method as compared to Euler's modified but RK-4 method gives better result among above three. Same observation is notices when h=0.05 and 0.01. The importance of RK-4 method is that it fits best in all cases. When decreasing the step size, h to be so small that absolute errors or round-off errors started to increase the accuracy, the calculations become very cumbersome for large values of n or alternatively large no. of step size; in other words we can say that the small value of h gives the better result for above methods. For RK-4 method at h=0.01 the plot from exact solution and by approximations coincides it means RK-4 gives better result as compared to others. In this paper for all cases, it has been observed that the convergences rate of approximate solutions to exact solutions is not so high but the amount of error is high when the considering step size is comparatively large; here again RK-4 gains high accuracy. So it is the reason why we opt the small value of step size, h. From the graphs and tables we can observe it easily. So step size, h play very important role to reducing the errors. Figure 1 is obtained by solving the differential equation directly or by ode command using Scilab. In figure 2(a)-2(c) the value of step size, h is 0.1; for figure 3(a)-3(c) the value of step size, h is 0.05 and finally for figure 4(a)-4(c) the step size, h is taken 0.01. The curve of figures 1 is same as obtained by approximations shown in other figures. Finally, it has been observed that we can reach up to the accurate solutions of IVPs of ODEs by utilizing the approximations methods when the step size is so much small. Finally, the result comes out in favour of RK-4 for high accuracy among all.

4. Conclusions: Finally, the results are calculated and tabulated with approximation solution. Exact Solution and absolute errors done using Scilab coding. RK-4 method fits best in all cases; it is more effective while comparing to other numerical methods as it reduces the minimum error. Finally, the results of high accuracy found in favour of RK-4 among all. In all cases the role of step size, h is very important and if it is low then accuracy goes to high or in other words we can say that smaller value of step size, h is needed for better result. The best value of the solution is found to be at x=0.4 in all cases. We can take different value of step size, h. The curve of figure 1 as obtained by direct solution is same as by approximations for all three methods. The results have been compared and it has been found that RK-4 method gives best result among all for smaller h. It controls the accuracy and adjustment of the step size. All the graphs have been plotted using Scilab. It has an advantage that is free of cost, open-source and easily available to all for any operating systems. RK-4 has some applications. It having much applications in Mechanics, aerodynamics and in non-linear dynamics etc. and in was This method was adopted in the study of fluid mechanics where some applications on laminar and turbulent aerodynamics (fully implicit schemes) described by M.H. et al. in 2005. Finally, a turbulent Navier- Stokes used to show the nature of order reduction that encountered in high Reynolds number applications [19]. RK-4 was used for solving a set of non-linear transcendental power flow equations of power and the feasibility of this method is tested on 5-bus, IEEE 14-bus, 39-bus and 57-bus test system. this method is capable to obtain the global optimal solution of each power network by solving the dynamics of HNN. The operations of an analog RC electrical circuit can be analyzed using RK-4 method [20].

Conflict of Interest: Authors declare No conflicts of interest.

5. References:
[1] Revathi. R. et al, Multicolored Approaches for Ordinary Differential Equation using Scilab, Journal of Propulsion Technology, 45 (2), 2024,1977-1985.
[2] Nur Shahirah Zulkifli et al, Improving Euler Method using Centroidal-Polygon Scheme for Better Accuracy in Resistor Capacitor Circuit Equation, J. Phys.: Conf. Ser. 2319 012023, 2022, 1-9.
[3] Ravindra Singh et al, The Study of A System of Non-Homogeneous Equations Using Matrix Exponential Method and Analysis With Scilab Software 6.1.1, J. Phys.: Conf. Ser. **2223** 012001, 2022, 1-12.
[4] M. A. Arefin at.el , Accuracy Analysis for the Solution of Initial Value Problem of ODEs Using Modified Euler Method, I. J. Mathematical Sciences and Computing, 7(2), 2021, 31-41.
[5] P. L. Sharma & A. Kumar, Demonstration Study on Runge-Kutta Fourth Order Method by Using MATLAB Programming, IOSR Journal of Mathematics 17(4), 2021, 1-9,
[6] P. Yaswanth & L. Naveen, Numerical Solution of Ordinary Differential Equation using Scilab, International Journal of Scientific Development and Research, 4(10), 2019, 93-97.
[7] V. Nirmala *et al*, Application of Runge-Kutta method for finding multiple numerical solutions to intuitionistic fuzzy differential equations, J. Phys.:Conf. Ser. 1139 012012, 1139, 2018, 1-8.
[8] S. N. Kumar et al, A Study on Application of Runge- Kutta Method with Respect to Traffic Flow Problem, Journal of Emerging Technologies and Innovative Research (JETIR), 6(6), 2019, 121-126.
[9] V. Chauhana & P. K. Srivastavab, Computational Techniques Based on Runge-Kutta Method of Various Order and Type for Solving Differential Equations, International Journal of Mathematical, Engineering and Management Sciences 4(2), 2019, 375–386,
[10] G. C. Paul & S. S. Kumar, Exploration on initial structures of extrasolar

protoplanets via new explicit RKAHeM(4.4) method, The Egyptian Journal of Remote Sensing and Space Science, 18(1), 2015, 1-8.

[11] S. A. Agam & Y. A. Yahaya, A highly efficient implicit Runge-Kutta method for first order ordinary differential equations. African Journal of Mathematics and computer science research.7(5), 2014, 55-60.

[12] S. S. Kumar & G. C. Paul, Application of new RKAHeM(4.4) technique to analyze the structure of initial extrasolar giant protoplanets, Earth Science Informatics, 5(1), 2012, 23-31.

[13] M. Podisuk, International Journal of Mathematical Models and Methods in Applied Science, 5(2), 2011, 387-394.

[14] Steven C. Chapra & Raymond P. Canale, Numerical Methods for Engineers, Mc Graw Hill, International Edition (6th Edition), 2010, ISBN 978–0–07–339792–4.

[15] D. Houcque, Matlab Application Ordinary Differential Equation, MathWorks Inc. 2010, 1-12.

[16] S. C. Chapra & R. P. Canale, Numerical Methods For Engineers, McGraw Hill, New York Edition-5, 2006. ISBN: 0071244298.

[17] S. Rao, Applied Numerical Methods for Engineers and Scientist, Pearson Prentice Hall Education, 2002, ISBN: 978-0130894809.

[18] Gilbeto. E. Urroz, Ordinary Differential Equations with SCILAB, Infor Clearinghouse.com, 2001.

[19] M. H. Carpanter et.al., Fourth-Order Runge–Kutta Schemes for Fluid Mechanics Applications, Journal of Scientific Computing, 25(1), 157-194, 2005.

[20] V. Veerasamy et.al., A novel RK4-Hopfield Neural Network for Power Flow Analysis of power system, Applied Soft Computing, 93, 2020, 106346

Estimation of Radiation Dose from Uranium Mill Tailings Bricks Used as Construction Material

Abhigyan[1], Gopal P. Verma*[1,2], Ranjan Prakash[1], Kumaraswamy V.[1], B. Naresh[1], Pallavi Singhal[1,2], and S.K. Jha[1,2]

[1]*Health Physics Division, Bhabha Atomic Research Centre, Trombay, Mumbai – 400 085, India*
[2]*Homi Bhabha National Institute, Trombay, Mumbai – 400 085, India*

*Corresponding Author E-mail: gpv@barc.gov.in

Abstract: In this study estimation of radiation dose from the bricks which are made of uranium mill tailings (UMT) was carried out. For this purpose, RESRAD-BUILD software was used for simulation of radiological exposure of occupant in a model room made with UMT bricks of various composition. In this study, standard model room having dimensions of 5 m × 4 m × 2.8 m was considered for computation. Its floor and ceiling are built with concrete, and the walls are made by using UMT bricks. The occupant location was considered at the centre of the room at 1m height from floor. Possible pathways of exposure were external exposure and inhalation of radon and progeny. The excess dose to occupant residing in model house made by UMT bricks had been found out to be 1 mSv for composition of UMT less than 20%. Further, radon concentration inside the room attributable to UMT bricks was found to be 6.5 – 32.2 Bqm^{-3} for UMT composition 10%-50% which is much less than the recommended action level for radon.

Keywords: Uranium mill tailings, Dwellings, RESRAD, Tailings bricks, Radon, Gamma, Dose.

1. Introduction:

Nuclear energy has played a significant role in achieving energy requirements worldwide. With the increase in demand for clean energy sources to reduce carbon emissions, nuclear energy has emerged as the most viable and robust option. Uranium mining and its extraction from natural deposits have been carried out for the past several decades for use in the production of electricity in nuclear power plants [1]. In India, Uranium mining started in the year 1967 in Jaduguda, Jharkhand [2]. At present, there are seven Uranium mines at Jaduguda, Bhatin, Narwapahar, Bagjata, Mohuldih, Turamdih and Banduhurang in Singhbhum East district in the eastern state of Jharkhand and one underground mine at Tummalapalle in Kadapa district of Andhra Pradesh. Additionally, two Uranium ore processing plants are operational at Jaduguda and Turamdih in Jharkhand which use acid leaching for extraction of U from ore, whereas one Uranium ore processing plant is operational at Tummalapalle in Andhra Pradesh which uses alkaline leaching for extraction of U from ore.

Upon extraction of U, low specific activity waste, known as Uranium mill tailings (UMT) generated in large volume is transferred in the form of slurry on a near surface engineered, designed tailings pond. The liquid part of the slurry is decanted and pumped back to the plant for reuse. The solid part of the slurry is impounded on the tailings pond for long term containment. Due to the presence of low ore grade (0.04% U_3O_8) Uranium deposits, almost the entire volume of processed ore emerges as waste. UMT contains residual amounts of U and all other radionuclides of the U decay series. Tailings

ponds can contribute to public exposure through radon exhalation and wind erosion of particulates. If not managed properly, it can also contribute to the contamination of adjoining groundwater bodies. Thus, long term monitoring is necessary to ensure the stability and integrity of the tailings pond. The tailings pond covers a large area of land which becomes unsuitable for any other purpose. To avoid these issues, and to ensure the sustainable operation of the Uranium industry, utilization of UMT for other purposes is required. UMT contains residual amounts of U and other natural radionuclides, so it is necessary to assess the radiological risks associated with its utilization. This present study was carried out to simulate the radiological exposure of an occupant residing in a dwelling made from bricks of uranium mill tailings.

2.   Material and methods
In this study a model room of dimensions 5 m $\times$ 4 m $\times$ 2.8 m was considered in which the floor and ceiling are made of concrete and walls are constructed from bricks made by UMT mixed with components of mixed fly ash bricks (MFAB). MFAB is composed of fly ash, sand, stone chips and gypsum. The radioactivity concentration of natural radionuclides in UMT and MFAB was analysed by using NaI(Tl) gamma-ray spectrometer. The data of radioactivity content and various other input parameters were used to simulate the dose inside the model house by using the RESRAD-BUILD computer code.

2.1 Natural radioactivity analysis
A total of 8 Uranium mill tailings (UMT) samples were collected from the tailings pond of Tummalapalle and 3 mixed fly ash brick (MFAB) samples were collected from local vendors. Samples were homogenized to reduce variance and were air dried, minced, crushed, and passed through a 2 mm mesh sieve [3]. The samples were analyzed for activity of the radionuclides ^{226}Ra, ^{232}Th and ^{40}K using NaI(Tl) gamma-ray spectrometer [4,5].

Samples were packed and sealed in plastic bottles of 250ml capacity and stored for 28 days so that the progeny of radium and thorium attain secular equilibrium with their daughter products. The energy calibration of the detector was done by using ^{137}Cs (662 KeV) and ^{60}Co (1173 & 1332 KeV) sources [6]. The efficiency calibration was done by using standard IAEA sources RGU, RGTh & RGK. The detector was kept in lead shielding of 4cm thickness to reduce the background. The samples were counted for 10000s. ^{226}Ra activity measurement was carried out by the gamma energy peak 1764 Kev of its daughter ^{214}Bi. ^{40}K activity was measured by its gamma peak of 1460 KeV. ^{232}Th activity measurement was carried out by the gamma energy peak 2614 KeV of its daughter ^{208}Tl [7,8]. The activity of a radionuclide was then calculated using Eq (1)

$$\text{Activity (Bq/kg)} = \frac{N \times 100 \times 100}{(T \times \gamma \times \eta \times W)} \qquad (1)$$

where, N= Background subtracted net counts, T = Counting time (sec), γ = Gamma emission probability in %, η = Efficiency for the particular gamma energy in % and W is the weight of the sample in kg.

2.2   Simulation   of   radiological exposure   using   RERRAD-BUILD Computer code
RERSAD-BUILD computer code was used for the simulation of radiological exposure of the occupant in a model room made with UMT bricks. RESRAD-BUILD developed by Argonne National Laboratory is a pathway model developed to assess the exposure of individuals resulting from occupancy in a contaminated building with radioactive materials [9, 10]. It is a member of RESRAD family computer codes which is used by regulatory authorities and universities in more than 100 countries for dose and risk calculations. RESRAD-BUILD computer code is capable of calculating the external radiation dose arising from radiation sources, inhalation doses from suspended dust and radon gaseous and ingestion doses from suspended radioactive particles. The code allows considering up to 10 sources of contamination within the building which can be point source, line source, area source or

volume source (contaminated wall). Building geometry can be chosen as starting from a single room to multiple rooms or storey up to three compartments. Dose for multiple receptors can be calculated at different locations inside the building. The code provides an option for introducing shielding between the source and receptor.

The exposure pathways provided in RESRAD-Build include external and internal exposure which are mentioned below:
- External exposure to radiation emitted directly from the source.
- External exposure to radiation emitted from radioactive particulates deposited on the floors of the room.
- External exposure to radiation due to submersion in air borne radioactive particulates.
- Inhalation of airborne radioactive particulates.
- Inhalation of aerosol indoor radon decay products.
- Inadvertent ingestion of radioactive material contained in removable material directly from the source.
- Inadvertent ingestion of airborne radioactive particulates deposited on the surfaces of the building.

Out of these possible exposure pathways, the major contributors are external

exposure to radiation emitted directly from the source and inhalation of radon and its progeny. These two pathways have been considered for the estimation of dose to the receptor.

In this study, a standard model room of dimensions of 5 m × 4 m × 2.8 m was considered. Its floor and ceiling are built with concrete. The walls of the room are made from bricks of UMT mixed with MFAB, which is the volume source of exposure to the receptor. The walls are plastered on both sides with concrete which acts as shielding between the source and the receptor. The thickness of the wall is 26 cm (23cm brick + 1.5cm plaster on both sides). The room has one door of dimensions 81" x 40" and two windows of dimensions 60" x 48". The receptor location is at the center of the room at a height of 1m from the floor. The indoor fraction of occupation is 0.8. Model realization of the room is shown in Fig 1. The receptor is shown in the middle of the room and the shapes numbered 1 to 4 represent the walls which are the rectangular volumetric radiation sources.

2.3 Estimation of external dose

The model for calculating external dose from the volume source (brick) is based on a semi-infinite slab source, with corrections for geometrical factors. The effective external dose D_{ex} from exposure to
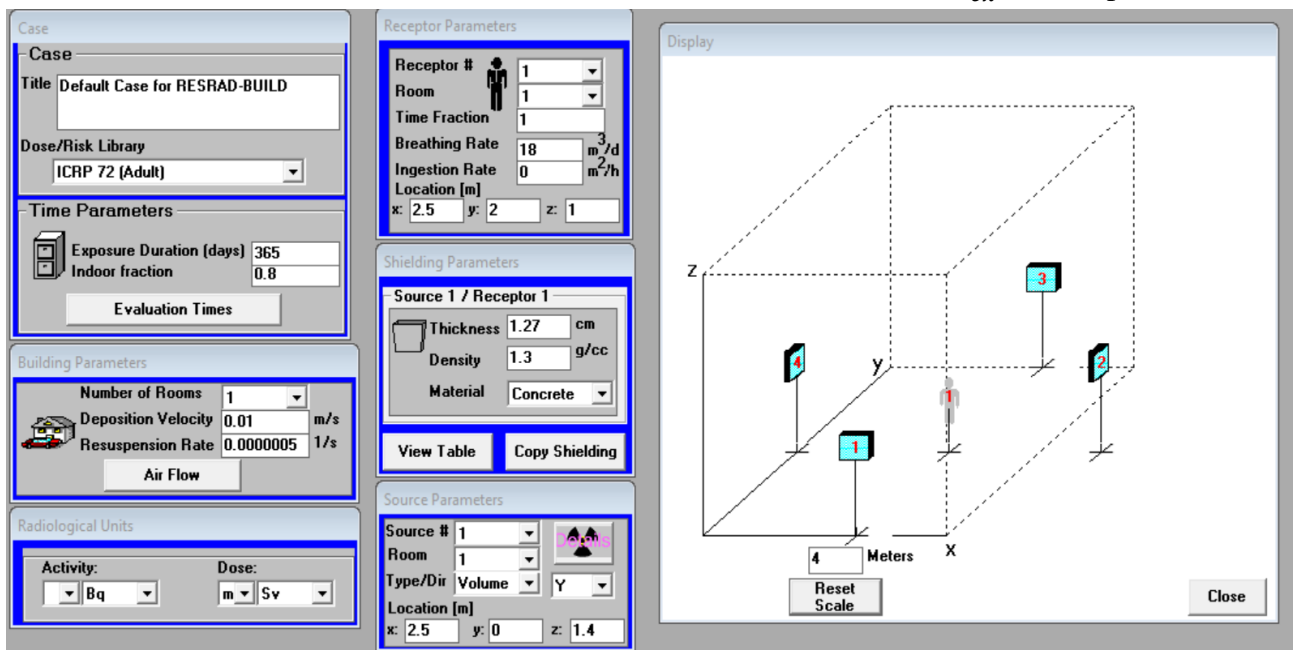

Figure 1. Room model in RESRAD-BUILD.

the source containing radionuclide n, is calculated by Eq. (2) [9]:

$$D_{ex} = ED * F_{in} * C_n * DCF_n * F_G^n \qquad (2)$$

where ED is exposure duration (years), F_{in} is the fraction of time spent indoors, C_n is the concentration of radionuclide n (Bq kg^{-1}), DCF_n is dose conversion factor $\{(mSvy^{-1})(Bqkg^{-1})^{-1}\}$ and F_G^n is geometric factor which takes into account area factor for finite area, source thickness, shielding, source material and position of receptor relative to the source for radionuclide n.

2.4 Estimation of indoor radon concentration and internal dose

A major portion of dose received by the receptor is due to the inhalation of short-lived progenies of ^{222}Rn. Radon is an inert gas which is a daughter product of ^{226}Ra. The radioactive decay of ^{226}Ra present in the UMT bricks leads to the formation of ^{222}Rn, which escapes out from the pores of brick matrix to the room. ^{222}Rn concentration inside the room was modeled by using air quality model. The radon concentration inside the room can be calculated by Eq. (3):

$$V_i \frac{dC_i^{Rn}(t)}{dt} = A_s J(t) - ((\lambda_{rn} + \lambda_v) V_i C_i^{Rn}(t) \qquad (3)$$

where $C_i^{Rn}(t)$ is concentration of Radon-222 at time t, $J(t)$ is radon flux through the exposed wall area at time t, λ_{rn} and λ_v are radioactive decay constant for radon (0.007 h^{-1}) and air exchange rate (h^{-1}) respectively, V_i is volume of the room (m^3), A_s is surface area of the walls (m^2)

The mass balance equation for radon activity in a two-phase medium consisting of solid and gas phase (no moisture) in the brick matrix can be represented by Eq (4):

$$\frac{\partial(\eta C_i^{Rn}(t))}{\partial t} = -\vec{\nabla} x \vec{J_m}(t) - \eta \lambda_{rn} C_i^{Rn}(t) + \eta \varepsilon \rho_s C_i^{Ra}(t) \lambda_{Rn}(\frac{1-\eta}{\eta}) \qquad (4)$$

where $C_i^{Ra}(t)$ is activity concentration of ^{226}Ra in brick at time t, $\vec{J_m}(t)$ is radon flux

through the matrix, η is volumetric porosity, ε is radon emanating factor, ρ_s is the density of solid phase of the porous medium.

In the absence of convective flow of the gaseous phase in the porous medium, the radon flux can be expressed by the Fickian diffusion equation:

$$\vec{J_m}(t) = -nD_e \vec{\nabla} C_i^{Rn}(t) \qquad (5)$$

where D_e is the diffusion coefficient of radon

Eq (5) and Eq (4) are combined and solved for steady state to compute radon concentration profile inside the matrix. The flux density at boundaries can be obtained by substituting the radon concentration profile to Eq (5) and solving at boundary condition. The obtained radon injection rate can be substituted to Eq (3) to obtain the radon concentration inside the room which can be used to calculate radon progeny concentration by mass balance equation. Working level month (WLM) can be calculated by radon progeny concentration and the effective internal dose (D_{in}) can be computed by Eq (6):

$$D_{in} = K * WLM * DCF \qquad (6)$$

Where DCF is the dose conversion factor and K is multiplication factor to account for the extrapolation of doses from uranium mines to homes.

Total effective dose can be calculated by taking the sum of external and internal doses. The details of input parameters used for simulation in RESRAD-BUILD are presented in Table 1.

3. Results and Discussion

The average activity concentration of ^{226}Ra, ^{232}Th and ^{40}K in UMT was found to be 2657±131 Bqkg^{-1}, 15±3 Bqkg^{-1} and 458±15 Bqkg^{-1} respectively, whereas average activity of ^{226}Ra, ^{232}Th and ^{40}K in MFAB was found to be 68±2 Bqkg^{-1}, 51±3 Bqkg^{-1} and 376±9 Bqkg^{-1} respectively. In this study a total of six different compositions of brick were considered for dose simulation, as presented in Table 2.

Table 1. RESRAD-BUILD input parameters used for dose calculations.

Parameters	Values
Dose library	ICRP 72 (Adult)
Indoor/time fraction	0.8
Room dimensions	5 m × 4 m × 2.8 m
Thickness of wall	26cm (23cm brick + 1.5cm plaster on sides)
Density of brick	1.60 gcm^{-3}
Total surface area of walls (excluding doors and windows)	44.5 m^2
Volume of model room	56 m^3
Number of room/occupants	1/1
Breathing rate	18 m^{3}d^{-1}
Deposition velocity	0.01 ms^{-1}
Resuspension rate	5 x 10^{-7} s^{-1}
Occupant location in the room	Centre of the room at 1m height from floor
Shielding type	Concrete
Shielding thickness	1.27 cm
Shielding density	1.30 gcm^{-3}
Type of source	Volume
Source geometry	Rectangular
^{222}Rn diffusion rate	2 × 10^{-5} ms^{-1}
Radon emanation factor	0.1
Building air exchange rate	1 h^{-1}

The activity concentration of bricks is based on activity concentration of tailings and fly ash. Radium equivalent (Ra$_{eq}$) is a widely used parameter to assess the gamma radiation hazard to humans. Ra$_{eq}$ is defined according to the estimation that 1 Bqkg^{-1} of ^{226}Ra, 0.7 Bqkg^{-1}of ^{232}Th and 13 Bqkg^{-1} of ^{40}K produce the same gamma dose rate [11].

Ra$_{eq}$ is calculated by using Eq (7) and is presented in Table 2.

$$Ra_{eq}= C_{Ra}+ 1.43\ C_{Th}+ 0.07\ C_K \qquad (7)$$

Where C$_{Ra}$, C$_{Th}$ and C$_K$ are activity concentrations of ^{226}Ra, ^{232}Th and ^{40}K in Bqkg^{-1} respectively. Recommended limits for building **materials** are also based on Ra$_{eq}$ activity.

The bricks with UMT fall under Class 2 (Ra$_{eq}$ between 370 – 740 Bqkg^{-1}) and Class 3 (Ra$_{eq}$ between 740 – 2220 Bqkg^{-1}) as per recommendations for building materials based on Radium equivalent activity [12]. Thus, the UMT bricks are suitable as construction materials for industries, roads, bridges, and foundation of non-residential buildings.

The radiological dose to the receptor residing inside the model house with brick compositions mentioned in Table 2 and input parameters mentioned in Table 1 have been evaluated by the RESRAD-BUILD code. Additional dose to the receptor residing in the model room made by using UMT in bricks can be calculated by subtracting the background dose, i.e. dose due to MFAB. The estimated annual effective external, internal, and total doses to recipient in model house made by using MFAB are 0.13, 0.04 and 0.17 mSv respectively. Excess effective external, internal, and total dose are presented in Table 3. The excess dose rate and radon concentration above background are also provided in Table 3.

Table 2. Activity concentration in various brick composition and radium equivalent

Sl No.	Composition of brick	^{226}Ra (Bqkg^{-1})	^{232}Th (Bqkg^{-1})	^{40}K (Bqkg^{-1})	Ra$_{eq}$ (Bqkg^{-1})
1	50% UMT + 50% MFAB	1363	33	417	1438
2	30% UMT + 70% MFAB	845	40	400	930
3	25% UMT + 75% MFAB	715	42	396	803
4	20% UMT + 80% MFAB	586	43	392	675
5	15% UMT + 85% MFAB	456	45	388	548
6	10% UMT + 90% MFAB	327	47	384	421

Table 3. Excess radiation dose from tailings bricks used in construction of dwelling.

Sl No.	Composition of brick	External dose (mSvy^{-1})	Dose rate (µSvh^{-1})	Internal dose (mSvy^{-1})	Radon conc. (Bqm^{-3})	Total dose (mSvy^{-1})
1	50% UMT + 50% MFAB	1.66	0.24	0.72	32.2	2.37
2	30% UMT + 70% MFAB	1.00	0.14	0.43	19.4	1.43
3	25% UMT + 75% MFAB	0.83	0.12	0.36	16.1	1.19
4	20% UMT + 80% MFAB	0.66	0.09	0.29	12.9	0.95
5	15% UMT + 85% MFAB	0.50	0.07	0.22	9.7	0.71
6	10% UMT + 90% MFAB	0.33	0.05	0.14	6.5	0.48

The increase in radon concentration inside dwelling due to use of UMT bricks ranges between 6.5 – 32.2 Bqm^{-3}, which corresponds to internal dose of 0.14 – 0.72 mSv, for indoor equilibrium factor of 0.4 [13].

Radon concentration is well within the recommended action level of WHO [14] and ICRP [15] of 150Bqm^{-3} and 200 Bqm^{-3} respectively. The increase in dose rate inside the dwelling due to use of UMT bricks ranges from 0.05 – 0.24 µSvh^{-1} which corresponds to external dose of 0.33 – 1.66 mSv. The additional total annual dose due **to** use of UMT bricks in place of mixed fly ash bricks ranges from 0.48 mSv to 2.37 mSv for the given compositions. The measured background average gamma dose rate and radon conc. in dwellings around Tummalapalle are 0.16 µSvh^{-1} and 19.9 Bqm^{-3} respectively which corresponds to a dose of 1.16 mSv and 0.44 mSv respectively. For UMT composition of 25%, the dose rate including background comes out to be 0.28 µSvh^{-1} which is comparable to indoor gamma radiation levels of 0.30 µSvh^{-1} for dwellings as per the recommended a limit of the Swedish National Board of Housing, Building, and Planning [16]. External dose to dweller is found to be less than 1mSv when the percentage composition of UMT is less than 25% and total dose, when percentage

composition of UMT is less than 20%, is less than the public dose limit of 1mSv.

4. Conclusions

The average activity concentration of ^{226}Ra, ^{232}Th and ^{40}K in UMT was found to be 2657±131 Bqkg^{-1}, 15±3 Bqkg^{-1} and 458±15 Bqkg^{-1} respectively, whereas average activity of ^{226}Ra, ^{232}Th and ^{40}K in MFAB was found to be 68±2 Bqkg^{-1} , 51±3 Bqkg^{-1} and 376±9 Bqkg^{-1} respectively. The radium equivalent of the six compositions of bricks ranges between 421 – 1438 Bqkg^{-1}. As per the recommendation based on radium equivalent, UMT bricks fall under Class 2 (Ra$_{eq}$ between 370 – 740 Bqkg^{-1}) and Class 3 (Ra$_{eq}$ between 740 – 2220 Bqkg^{-1}), thus, the UMT bricks are suitable as construction materials for industries, roads, bridges, and foundation of non-residential buildings. Additional dose due to the use of UMT bricks ranges from 0.48 mSv to 2.37 mSv. The additional radon concentration ranges from 6.5 – 32.2 Bqm^{-3}, which is well within the recommended action level. For computational purposes, 1 air change per hour was considered. Air changes per hour can be increased to further decrease the internal dose. External dose to dweller is found to be less than 1 mSv when the percentage composition of UMT is less than 25% and total dose is less than the public dose limit of 1 mSv when percentage

composition of UMT is less than 20%. Thus, based on the input parameters considered for computation, bricks with UMT composition less than 20% are safe for use as construction material.

5. Acknowledgements

References

1. Bhattacharjee B, In 14thIndian Nuclear Society Annual Conference (INSAC), IT-1, 1–27, 2003
2. Gupta, R. and Siddique, S, Management of the tailings and liquid effluents in uranium mining and milling operations. Radiation Protection and Environment, 26(3 & 4), (2003), 506 -515.
3. Operating Procedure, Soil Sampling. IAEA, Soil sampling for environmental contaminants. IAEA TECDOC-1415, International Atomic Energy Agency, Vienna, 2004
4. M. Condomines, O. Loubeau and P. Patrier, Recent mobilization of U- series radionuclides in the Bernardan U deposit (French Massif Central). Chem. Geol., 244 (2007) 304–315.
5. V.K. Shukla, S. Chinnaesakki, A.A. Shanbhag, S.J. Sartandel, G.K. Srivastava, A.H. Khan and V.D. Puranik, Proceedings of the National Symposium on Environment (2004) 445–448.
6. Knoll, G. F.,Radiation Detection and Measurement, 3rd edition, Wiley, ISBN 978-0471073383, 1999.
7. García-Talavera, M., Evaluation of the suitability of various γ lines for the γspectrometric determination of 238U in environmental samples. Appl. Radiat. Isot., 59, (2003), 165-173.
8. Morillon, C., Bé, M.M., Lamé, J., Jean, C., Nucléide- Lara. ISBN 2-7272-212-1, CEA-LNHB, Saclay, 2000
9. Yu C., LePoire, D.J., J.-J. Cheng, E. Gnanapragasam, S. Kamboj, J. Arnish, B.M. Biwer, A.J. Zielen, W. a. Williams, a. W. Iii, H.T. Peterson Jr., User's Manual RESRAD-BUILD Version 3, 2003.
10. Pepin, S., Using RESRAD-BUILD to assess the external dose from the natural radioactivity of building materials, Construct. Build. Mater. 168 (2018) 1003e1007.
11. UNSCEAR, Sources and Effects of Ionising Radiation, United Nations. Report toGeneral Assembly with Scientific Annexes. United Nations, New York, 2000
12. Oresegun, M.O., Babalola, A.I., In: Proceedings of an International Conference on Radiation Protection in Nuclear Energy, vol. 2. 18–22 April, IAEA, Vienna, Austria, pp. 159–166 (1988). Available at: https://inis.iaea.org/collection/NCLColle ctionStore/_Public/20/026/20026283.pdf. (last accessed 20 September 2023).
13. UNSCEAR, United Nations Scientific Committee on the Effect of Atomic Radiation. Sources and biological effects of ionizing radiation. United Nations, New York, 1993
14. WHO Handbook on Indoor Radon. A Public Health Perspective. World Health Organization, Geneva (2009).
15. Lecomte, J.-F.; Solomon, S.; Takala, J.; Jung, T.; Strand, P.; Murith, C.; Kiselev, S.; Zhuo, W.; Shannoun, F.; Janssens, A., ICRP Publication 126: Radiological Protection against Radon Exposure. Annals of the ICRP, 43(3) (2014), 5–73.
16. Building Regulations, Mandatory provisions and general recommendations, Section 6 Hygiene, health and the environment, Code of Statutes of the Swedish Board of Housing, Building and Planning. BBR 2006:22.

Disease Detection using Artificial Neural Network

M. Kate, S. Jangam, T. Pitale, S. Patil, S. Garani[1], Subhrodipto B. Choudhury[2*]

Artificial Intelligence and Data Science, ISBM COE, Pune, Maharashtra, India
[1]Dept. of Fishery Science, WBUAFS, Kolkata, West Bengal
[2] Dept. of E & TC, ISBM College of Engineering, Pune, Maharashtra

Corresponding Author Email: bumbadit@gmail.com

Abstract: Artificial Neural Networks (ANNs) have emerged as a transformative technology in the field of medical diagnostics, demonstrating significant potential in disease detection. This study highlights the application of ANNs in identifying complex diseases such as cancer, diabetes, and cardiovascular disorders. By analysing diverse datasets comprising clinical, demographic, and imaging data, ANNs effectively detect disease patterns and predict severity, aiding early diagnosis and treatment planning. Advanced methodologies, including feature extraction, image analysis, and cross-validation, were employed to optimize model accuracy and generalizability. Despite achieving high accuracy rates, challenges such as data quality, interpretability, and computational demands persist, necessitating further research. The findings underscore the importance of ANNs in modern healthcare, offering a promising pathway for improved diagnostic precision and patient outcomes while emphasizing the need for advancements in data management, ethical considerations, and model interpretability.

1. Introduction: Detection of medical ailment has been an important topic in present day research. Disease is usually caused by micro-organisms like bacteria, virus, etc. hence detection and intensity of the disease has to be measured to take preventive and corrective action against the disease.

Cancer is generally caused by abnormal growth of cell in human body. Early detection and measurement of intensity helps in taking medical assistance for curing from it. Analysis of image of human cell extract relevant features. These features are checked with features of un-diseased human cell to get into the conclusion.

1.1. Artificial Neural Network

Artificial Neural Networks (ANNs) are computational models inspired by the biological neural networks of the human brain. These networks consist of interconnected nodes, or neurons, organized in layers. Each neuron receives input, processes it, and then passes the result to the next layer of neurons. ANNs have shown remarkable capability in pattern recognition and classification tasks, making them valuable tools in medical research and diagnosis [1].

In the context of disease detection, ANNs can analyze complex medical data such as imaging scans, genetic information, or patient records to identify patterns indicative of various diseases. By training ANNs on large datasets containing both healthy and diseased samples, researchers can develop models capable of accurately detecting diseases at early stages, aiding in timely interventions and improving patient outcomes. The ongoing advancements in ANNs and their applications in healthcare

underscore their potential to revolutionize disease diagnosis and treatment [2,4].

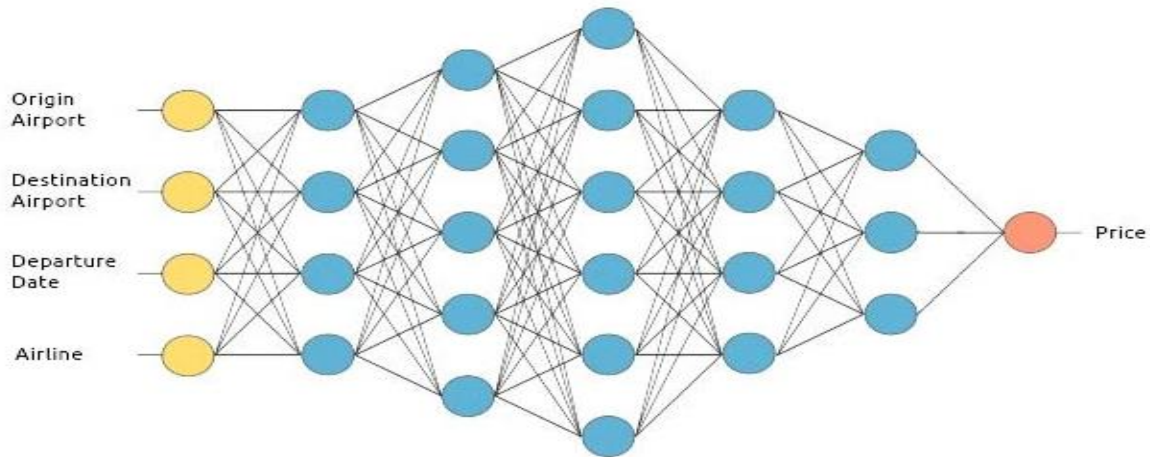as cough and breath sounds, to diagnose conditions like COPD and asthma with high

Figure 1. Architecture of Artificial Neural Network (ANN) (Source: 8 Best Deep Learning Tools and Applications in 2024)

Currently, data driven AI assisted system helps in extraction of features that are fed to neural network to predict the disease and its intensity. Predictive and prescriptive data analytic are playing in vital role these days in medical treatment. These help medical practitioners to take decision of treatment based on the result of AI assisted system.

Artificial Neural Networks (ANNs) have emerged as powerful tools for disease detection across various medical fields, significantly enhancing diagnostic accuracy and efficiency. By leveraging their ability to learn complex patterns from diverse datasets, ANNs can assist in early diagnosis and treatment, ultimately improving patient outcomes. The following sections outline the key applications of ANNs in disease detection. ANNs can analyze complex data patterns to identify heart disease risk factors, improving early diagnosis [4]. Integration of multimodal data sources, including ECG analysis, enhances the accuracy of predictions [4]. ANNs have demonstrated superior performance over traditional diagnostic methods, achieving high accuracy in liver disease detection [13]. The use of optimized ANN models has shown significant improvements in sensitivity and specificity, aiding clinical decision-making [13]. ANNs can process audio signals, such

accuracy [2]. his innovative approach complements image-based diagnostics, providing a multifaceted diagnostic tool [2].

ANNs can analyze vast amounts of medical data to identify disease patterns and predict outbreaks, enhancing public health responses [3]. Their ability to integrate diverse data sources allows for comprehensive disease risk assessments [3]. AI tools have emerged as pivotal assets in disease detection, enhancing the accuracy and speed of diagnoses across various medical fields. These tools leverage advanced algorithms and machine learning techniques to analyze vast datasets, enabling early identification of diseases such as cancer, Alzheimer's, and infectious diseases. The following sections outline key AI applications in disease detection.

1.2. Different AI tool used to analysis disease status

1.2.1. Deep Learning Algorithms: AI systems utilize deep learning to analyze medical records and genetic data, identifying individuals at risk for cancer [5].

1.2.2. Image Analysis: AI enhances image-based diagnostics through techniques like segmentation and feature extraction,

improving decision-making accuracy for complex diseases [6].

1.2.3. Hippocampus Analysis: Utilizing the VGG16 model, AI can classify patients into categories based on hippocampal imaging, achieving high accuracy in early detection [7].

1.2.4. Image Analysis Techniques: AI-driven methods refine medical imaging, facilitating accurate diagnoses of infectious diseases and enabling tailored treatment plans [8].

1.2.5. Real-Time Data Monitoring: AI analyzes diverse data sources to predict and monitor disease outbreaks, significantly improving public health responses [9].

1.3. Limitations of Using Artificial Neural Networks (ANNs) in Disease Detection

1.3.1. Data Quality and Quantity

Challenge: ANN performance heavily depends on the quality and size of the dataset. Medical datasets are often small, noisy, or imbalanced due to the difficulty of collecting labelled data, particularly for rare diseases. Insufficient or poor-quality data can lead to inaccurate predictions and limit the generalizability of models. Detecting rare conditions like certain genetic disorders may require data from a very small patient population.

1.3.2. Overfitting and Generalization

Challenge: ANNs, particularly deep learning models, are prone to overfitting, where the model memorizes the training data rather than learning general patterns. This reduces the model's ability to perform well on unseen data, especially when the training data lacks diversity. An ANN trained on data from a single hospital might fail to generalize to patients from different demographics or healthcare systems.

1.3.3. Model Interpretability (Black-Box Nature)

Challenge: ANNs are often criticized for their lack of transparency in decision-making. Clinicians and patients may be reluctant to trust a "black-box" system without clear explanations of how diagnoses are made. Limited interpretability can hinder clinical adoption and regulatory approval. Explaining why an ANN flagged a specific MRI scan as indicative of cancer remains difficult.

1.3.4. Computational Complexity and Resource Requirements

Challenge: Training and deploying large ANN models require significant computational resources, including GPUs and memory, which may not be available in resource-constrained settings. Impact: Limits the applicability of ANN solutions in rural or low-income regions. Deploying ANN-powered diagnostics in remote clinics with limited computational infrastructure can be infeasible.

1.3.5. Bias in Data and Algorithms

Challenge: Training data often reflects societal biases, such as underrepresentation of certain groups. These biases can be inadvertently learned by the ANN. Can lead to unequal performance across different demographic groups, raising ethical concerns. An ANN trained predominantly on data from male patients might perform poorly for female patients.

1.3.6. Ethical and Legal Concerns

Challenge: Handling sensitive medical data raises concerns about patient privacy, data security, and compliance with regulations like GDPR and HIPAA. Non-compliance can result in legal penalties and loss of patient trust. A breach in an ANN-powered diagnostic system could expose sensitive health information.

1.3.7. Variability in Data Sources

Challenge: Medical data varies significantly across regions and healthcare systems due to differences in equipment, protocols, and

demographics. ANN models trained on data from one region or system may not perform well in others. An ANN trained on MRI scans from one manufacturer might struggle to interpret scans from another.

1.3.8. Requirement for Domain Expertise

Challenge: Designing and training ANNs for disease detection often requires collaboration between AI experts and medical professionals. Misaligned objectives or misinterpretation of medical data can lead to flawed models. Increases the complexity and cost of developing ANN solutions. Incorrect preprocessing of imaging data could lead to suboptimal model performance. While these limitations present obstacles, they also highlight areas where innovation can drive significant improvements in healthcare AI applications.

ANNs show great promise in disease detection, challenges such as model interpretability and the need for extensive training data remain. Addressing these issues is crucial for the broader adoption of ANNs in clinical settings. In this work we try to implement AI validation protocols for improvement of different disease detection.

2. Methodology

Most of the cases the work flow going on by these mentioned processes:

A compilation of a comprehensive dataset containing diverse samples of both healthy individuals and those afflicted with the target disease. The dataset includes various demographic, clinical, and diagnostic parameters relevant to the disease under study.

Next, it was preprocessed the data to remove noise, handle missing values, and normalize features to ensure uniformity across the dataset. then design and train the ANN model, configuring its architecture, such as the number of layers and neurons, based on the complexity of the disease and the characteristics of the dataset. During the training process, we employ techniques like cross-validation to optimize hyperparameters and prevent overfitting. Finally, it was evaluating the performance of our model using metrics like accuracy, sensitivity, specificity, and area under the ROC curve to assess its effectiveness in disease detection.

3. Key findings from recent studies

In the realm of disease detection, Artificial Neural Networks (ANNs) have emerged as a potent tool, revolutionizing the landscape of medical diagnostics.

The accuracy of disease detection using Artificial Neural Networks (ANNs) has shown significant promise across various medical conditions. Research indicates that ANNs can achieve high accuracy rates,

Figure 2. Work flow as prepared

making them valuable tools for early diagnosis and treatment planning. The following sections highlight key findings from recent studies on ANN applications in disease detection.

3.1. Congenital Heart Disease Detection: An ANN model developed for detecting Congenital Heart Disease (CHD) achieved an impressive accuracy of 97.44%, outperforming Logistic Regression (95.00%) and Extreme Gradient Boosting (92.00%) [10]. This model utilized data preprocessing techniques such as imputation and Principal Component Analysis (PCA) to enhance performance.

3.2. Cardiovascular Disorders: Another study reported an ANN model achieving 94.15% accuracy in predicting heart disease, significantly surpassing the Logistic Regression baseline of 85.71% [11]. The methodology included comprehensive data preprocessing and evaluation techniques, underscoring the ANN's effectiveness in this domain.

3.3. Broader Applications: ANNs have also been applied to various diseases, including liver disease and COVID-19, with models achieving accuracies above 97% [12,13]. These models demonstrate the versatility of ANNs in handling complex datasets and improving diagnostic precision.

While ANNs show remarkable accuracy in disease detection, challenges such as data privacy, algorithm complexity, and the need for large datasets remain critical considerations for future research.

4. Challenges and Limitations

4.1. Data Quality and Quantity: The performance of ANNs heavily relies on the quality and quantity of the input data. Challenges may arise if the dataset is small, imbalanced, or noisy. Moreover, acquiring labeled data for training can be expensive and time-consuming, especially for rare diseases.

4.2. Feature Selection and Extraction: Identifying relevant features from the input data is crucial for the effectiveness of ANNs. However, selecting appropriate features and extracting meaningful information from raw data can be challenging, especially in complex datasets with high dimensionality.

4.3. Overfitting and Generalization: ANNs are prone to overfitting, where the model learns to memorize the training data instead of capturing underlying patterns. Achieving good generalization performance on unseen data is crucial for real-world disease detection applications.

4.4. Interpretability: ANNs are often considered as black- box models, making it challenging to interpret the underlying decision-making process. Lack of
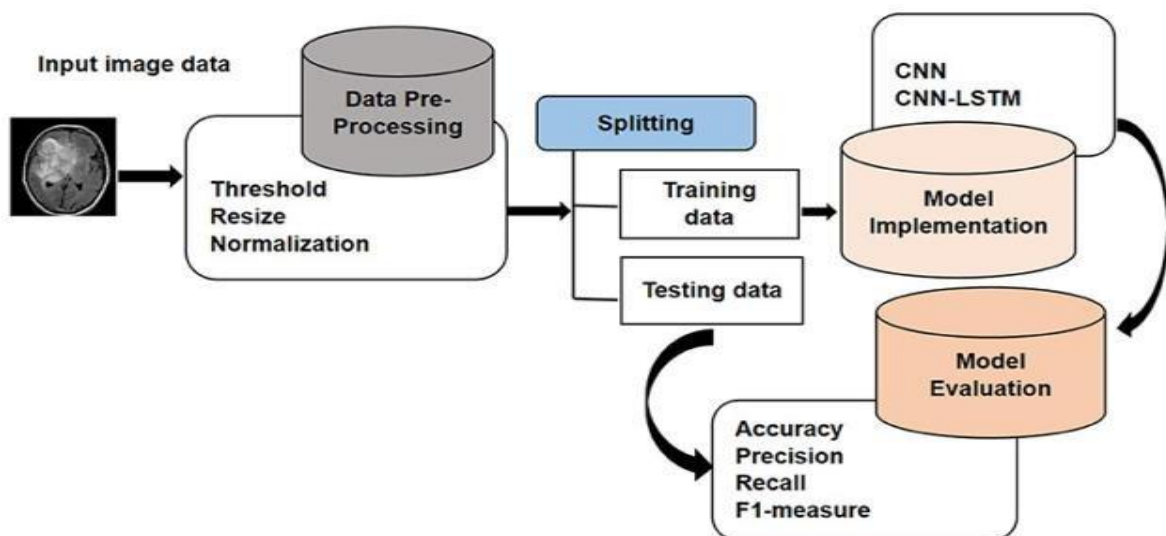

Figure 3. Feature extraction process (Source: https://www.frontiersin.org)

interpretability may hinder the trust and acceptance of these models by healthcare professionals and patients.

4.5. Model Complexity and Computational Resources: Training complex ANN architectures requires significant computational resources and time. Deploying such models in real-world settings, especially in resource-constrained environments like clinics or remote areas, can be challenging.

4.6. Robustness to Variability: ANNs may struggle to generalize well in the presence of variability in data due to factors such as demographic differences, environmental factors, or technological variations. Ensuring robustness to such variability is crucial for reliable disease detection.

5. Conclusions

Artificial Neural Networks (ANNs) hold immense promise in transforming the landscape of disease detection and medical diagnostics. Their ability to process complex and diverse datasets has enabled accurate identification of various diseases, such as cancer, cardiovascular disorders, and diabetes, at early stages, thereby improving the chances of successful treatment and better patient outcomes. The study demonstrated that ANNs achieve high accuracy and robust performance when trained on comprehensive and high-quality datasets, showcasing their versatility across medical domains.

However, several challenges persist that need to be addressed for wider adoption of ANNs

Figure 4. Disease detection using unsupervised learning (Source: https://www.semanticscholar.org)

4.7. Ethical and Legal Considerations: Implementing ANNs for disease detection raises ethical concerns related to patient privacy, data security, and potential biases in the algorithm. Compliance with regulations such as GDPR and HIPAA is essential to safeguard patient rights and data confidentiality.

4.8. Validation and Benchmarking: Proper validation and benchmarking of ANN models is necessary to assess their performance accurately. However, selecting appropriate evaluation metrics and comparison methods can be challenging due to the lack of standardized protocols in the field.

in clinical practice. These include the "black-box" nature of ANN models, which limits interpretability, the reliance on large, high-quality datasets, and the computational resources required for training and deployment. Ethical considerations, such as data privacy, fairness, and compliance with regulations like GDPR and HIPAA, are equally crucial to ensuring responsible implementation in healthcare.

To fully realize the potential of ANNs in disease detection, future research should focus on improving model interpretability, developing standardized validation protocols, addressing data-related biases, and optimizing models for resource-constrained environments. Additionally, fostering collaboration between AI experts and

medical professionals is essential to align technical innovations with clinical needs.

By overcoming these challenges, ANNs can become a cornerstone of precision medicine, significantly enhancing the efficiency and accuracy of disease detection and paving the way for more proactive and patient-centered healthcare systems.

NO confliction between all authors.

6. References

[1] Hemalatha, V., & Sundar, C. (2021). Retracted article: automatic liver cancer detection in abdominal liver images using soft optimization techniques. Journal of Ambient Intelligence and Humanized Computing, 12(5), 4765-4774.

[2] Türkçetin, A. Ö., Koç, T., & Çilekar, Ş. (2023, July). The Use of ANN in the Sound Detection of Lung Diseases: Example of COPD, Asthma, Pneumonia. In 2023 31st Signal Processing and Communications Applications Conference (SIU) (pp. 1-4). IEEE.

[3] Kumar, K. K., & Nasar I, S. (2024). Various Approaches and Applications of Artificial Intelligence in Preventing and Detecting Diseases.

[4] Dehankar, P., & Das, S. (2024). Detection of Heart Disease Using ANN: Present Research and Future Opportunities. Future of AI in Biomedicine and Biotechnology, 182-196.

[5] Hariharan, M. G., Saranya, S., Velavan, P., Soji, E. S., Rajest, S. S., & Thammareddi, L. (2024). Utilization of Artificial Intelligence Algorithms for Advanced Cancer Detection in the Healthcare Domain. In Advancements in Clinical Medicine (pp. 287-302). IGI Global.

[6] Rani, E. F. I., Pushparaj, T. L., & Raj, E. F. I. (2024). Computer-aided Bio-medical Tools for Disease Identification. Disease Prediction using Machine Learning, Deep Learning and Data Analytics, 52.

[7] Rehman, S. U., Tarek, N., Magdy, C., Kamel, M., Abdelhalim, M., Melek, A., ... & Sadek, I. (2024). AI-based tool for early detection of Alzheimer's disease. Heliyon, 10(8).

[8] Ahsan, M., & Damaševičius, R. (2024). Infection detection revolution: Harnessing AI-powered image analysis to combat infectious diseases. Plos one, 19(10), e0307437.

[9] Giri, P. A., & Gupta, M. K. (2024). Transforming Disease Surveillance through Artificial Intelligence. Indian Journal of Community Medicine, 49(5), 663-664.

[10] Ezigbo, L. I., Kwubeghari, A., & Okoye, F. (2024). Early Detection of Congenital Heart Diseases among Infants Using Artificial Neural Network Algorithm. ABUAD Journal of Engineering Research and Development (AJERD), 7(2), 436-445.

[11] Krishnamoorthi, V. (2024, April). Early Detection of Cardiovascular Disorders Using Enhanced ANN Model. In 2024 International Conference on Advances in Data Engineering and Intelligent Computing Systems (ADICS) (pp. 01-06). IEEE.

[12] Azeem, M., Javaid, S., Khalil, R. A., Fahim, H., Althobaiti, T., Alsharif, N., & Saeed, N. (2023). Neural Networks for the Detection of COVID-19 and Other Diseases: Prospects and Challenges. Bioengineering, 10(7), 850.

[13] Hemanth, D. J. (Ed.). (2023). Computational Intelligence and Modelling Techniques for Disease Detection in Mammogram Images. Elsevier.

CNS&E

Current Natural Sciences & Engineering

www.cnsejournals.org

e-ISSN
3048-460X

CNS&E Journal papers are widely available in Google Scholar, Research Gate and in other citation platforms.

Crossref

Globally Visible

Peer Reviewed

A Comprehensive Interdisciplinary Partially Open Access Journal

Easy Submission, Quick Publication in 40 days

CNS&E Journal assigns DOIs to published articles for international citation.

The journal uses Turnitin software to ensure originality and it provides readers with reliable, plagiarism-free scientific research.

CNS&E Editorial Board Comprises of Globally Renowned S & T Luminaries & Advisory Support from World Top Institutes' Leaders

Current Natural Sciences & Engineering (CNS&E), a bimonthly journal, publishes new, innovative and cutting-edge research in:

- Natural Sciences
- Health Science
- Nuclear science
- Agricultural Science
- Environmental Science
- Nanomaterials
- Hydrogen Energy
- Net Carbon Zero
- Industrial R&D
- Engineering & AI
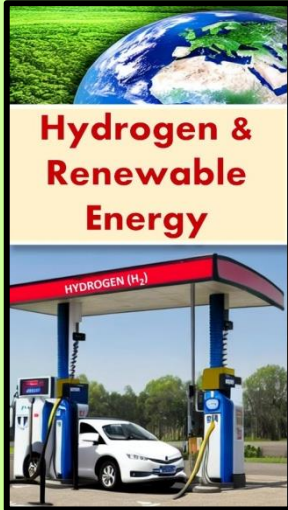
No Article Processing Charges !!!
For 3 months

The Most **Valuable & Biggest** Journal on **New Science** from **India**

A Unique Platform to Boost your Research Impact Globally !

CNS&E
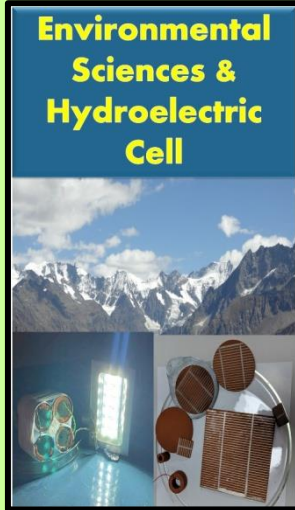
Current Natural Sciences & Engineering

Hydrogen & Renewable Energy
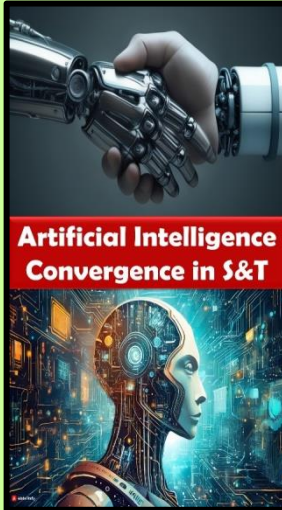
HYDROGEN (H₂)

Environmental Sciences & Hydroelectric Cell
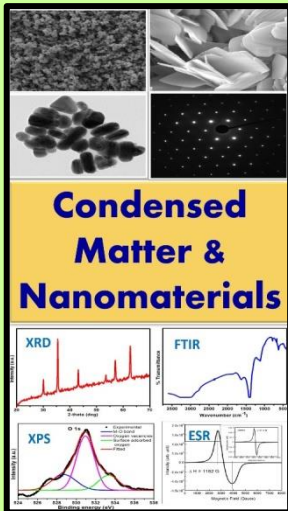
Artificial Intelligence Convergence in S&T

Net Carbon Zero & Earth Sustainability

Condensed Matter & Nanomaterials

XRD

FTIR

XPS

ESR
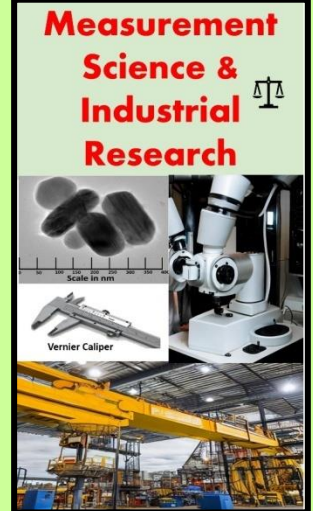
Health Science & Technology

Nuclear Science: Health & Society

Measurement Science & Industrial Research
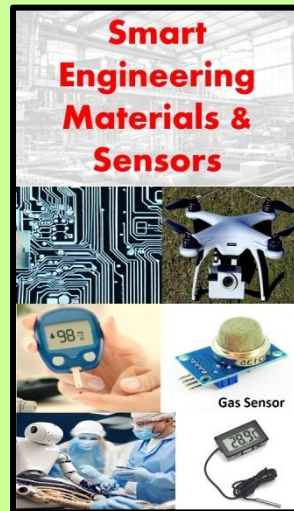
Scale in nm

Vernier Caliper

Digital & Sustainable Agriculture

Smart Engineering Materials & Sensors

Gas Sensor